AMERICAN UNIVERSITY OF BEIRUT

Thermal Properties Measurement Using Mirage-Effect Experiment

by
Mohammad Kazem Hadi

A thesis
submitted in partial fulfillment of the requirements
for the degree of Master of Science
to the Department of Physics
of the Faculty of Arts and Science
at the American University of Beirut

Beirut, Lebanon
May 2018

AMERICAN UNIVERSITY OF BEIRUT

Thermal Properties Measurement Using Mirage-Effect Experiment

by

Mohammad Kazem Hadi

Approved by:

Dr. Michel Kazan, Associate Professor — Advisor

Physics

Dr. Malek Tabbal, Professor — Member of Committee

Physics

Dr. Leonid Klushin, Professor — Member of Committee

Physics

Date of thesis defense: May 10, 2018

AMERICAN UNIVERSITY OF BEIRUT

THESIS, DISSERTATION, PROJECT RELEASE FORM

Student Name: Hadi Mohammad Kazem
Last First Middle

☑ Master's Thesis ○ Master's Project ○ Doctoral Dissertation

☐ I authorize the American University of Beirut to: (a) reproduce hard or electronic copies of my thesis, dissertation, or project; (b) include such copies in the archives and digital repositories of the University; and (c) make freely available such copies to third parties for research or educational purposes.

☑ I authorize the American University of Beirut, to: (a) reproduce hard or electronic copies of it; (b) include such copies in the archives and digital repositories of the University; and (c) make freely available such copies to third parties for research or educational purposes after:

One ___ year from the date of submission of my thesis, dissertation or project.
Two ___ years from the date of submission of my thesis , dissertation or project.
Three ☑ years from the date of submission of my thesis , dissertation or project.

Signature 10-05-2018
Date

This form is signed when submitting the thesis, dissertation, or project to the University Libraries

Acknowledgements

This thesis which is based on an experimental setup was done with a research grant from CNRS-Lebanon and AUB through URB. I want to thank my thesis advisor Prof. Michel Kazan for the support and time spent during my work and to the skills that I learned from him in dealing with the thesis problem and how to formulate a problem and analyze results. It is also my great pleasure to thank also my thesis committee members Prof. Malek Tabbal and Prof. Leonid Klushin for the time they spent in reading the thesis and for their discussions on the experiment which helped me in understanding the problem and light up on some important things I missed.

I would also like to present my appreciation to my friends Ms. Zeinab Harajli and Dr. Abdo Iskandar for their help during the experiment, and for the medical Engineering team responsible for maintenance of research machines in the physics department especially Mr. Joan Younes for their help in building the experiment and staying with me after their working hours which helped in finishing my experiments during this short time. Moreover, I want to thank the head of the machine shop Mr. Elie Melki for helping us in building some instruments for the experiment.

I want to thank my first friends at AUB Fatima Hussein and Mohammad Tohme for the help and support that they provided about the regulations and admission to AUB.

I want to thank Ms. Joumana Abi-Fallah and Dr. Samar Harkouss who also helped me in my admission to AUB. I also present my gratitude to AUB physics department for giving me a graduate assistant-ship that helped me in covering my tuition fees. Moreover, I can't forget the physics labs manager Ms. Elisar Majdalani for her support, help, monitoring, and advising she provided to me in teaching and mastering my lab duties.

I want to thank my academic advisors Prof. Mounib El-Eid and Prof. Jihad Touma for advising me on the academics and the education system at AUB.

I want to thank every instructor with whom I took my courses at AUB mainly Prof. Ali Chamseddine and Prof. Jihad Touma who changed my way of studying and thinking about problems.

I want to thank my graduate physics colleagues for the good time we spend with each other and for the discussions we always had. Moreover, my SRC's

colleagues and the Associate Provost Prof. Zaher Dawy for the time we spent in formulating the new GA policy. I should also acknowledge FAS Dean Prof. Nadia Cheikh, Associate Dean Prof. Bana Bashour, chair of graduate studies committee Prof. Samih Isber, Ms. Leila Knio, Ms. Abeer Khoury, and Ms. Rima Rassi for the time they provided for dealing with students problems and accepting our ideas.

At the end, I want to thank my family for the emotional support during the hard time that I passed during my study.

An Abstract of the Thesis of

Mohammad Kazem Hadi for Master of Science
Major: Physics

Title: Thermal Properties Measurement Using Mirage-Effect Experiment

The analysis of the heat transport in insulator crystals has always been the focus of research because the knowledge that can be gained on the fundamental physical mechanisms governing the heat transport can help in the development of efficient thermal management strategies for many technological applications. Thermal properties of materials usually give us practical information about its properties. Experimental measurement of thermal properties is the main subject for this thesis. We built a Mirage-Effect experiment to measure thermal properties of materials where its main concept is to focus a modulated heat source on the surface of the sample. As heat is absorbed, it will create a temperature gradient arising in the gas near the surface which will create a gradient of refractive index of the gas. This gradient is detected by another probe laser skimming the surface of the heated spot where the deflection of this probe beam is detected through a four position detector. The main concept of the experiment is based on generating thermal waves on the surfaces of the elaborated samples. These waves are determined by the thermal properties of the samples. Their propagation in the air just above the boundary will create a gradient of refraction index in the air. This will allow the probe laser beam to deflect. The deflection of the probe laser beam as a function of the distance from the heating spot will allow the determination of the thermal properties of sample under consideration. The deflection of the probe beam has two components:transverse and normal. We do a multi-parameter fit of the experimental results with the expression of the deflection where we can deduce the values of thermal diffusivity and thermal conductivity of the material.

We also measure the thermal diffusivity and thermal conductivity of a set of silicon carbide samples characterized by different dozes of proton bombardment in order to study the effect of bombardment of protons on the thermal efficiency of SiC.

Contents

List of Figures

Chapter 1

Introduction

The study of thermal properties of materials has witnessed technological breakthroughs since the development of microelectronics and nanotechnology. The reason is that the reduction of the electronic devices should be accompanied with an efficient thermal management strategy to prevent the failure of the device. In what follows we describe the fundamental of physics heat transfer.

1.1 Fundamental Laws of Heat Transfer

Heat can be transferred through materials via conduction, convection, or radiation. The three heat transfer processes are described below [1].

1.1.1 Heat Transfer by Conduction

The most important quantity describing the heat transfer is the thermal conductivity, which is defined as the rate of energy transfer per unit length between two point of temperature difference of 1K. The transfer of heat through one material is called heat transfer by conduction. This type of heat transfer is described by the Fourier law which relates the energy density of the heat flux $\mathbf{j}$ to the applied temperature gradient on the sample.

$$\mathbf{j} = \kappa \nabla T \tag{1.1}$$

Here κ is the thermal conductivity of the material.
Using the equation of conservation of energy we can find the time-position evolution of temperature by the following equation:

$$\frac{\partial T}{\partial t} = \frac{\kappa}{\rho c_p} \nabla^2 T \tag{1.2}$$

The coefficient of the Laplacian of temperature is known as the heat diffusivity $\alpha = \kappa / \rho c_p$, with ρ being the density of the material and c_p its heat capacity at

constant pressure. The thermal diffusivity α is defined by the ratio $\kappa/\rho c_p$. The latter is related to the ability of the material to diffuse energy by conduction.

In the macroscopic scale, Fourier assumes instantaneous response of the system to the temperature gradient. In this case the response time of the system is very short and considered negligible compared to the time of observation.

1.1.2 Energy Transfered by Convection

Macroscopic movement of molecules within the fluid is the main mode of energy transfer in fluids. This is known as convection. In fluids, molecules can freely move unless their mean free path is affected by their intermolecular collisions. There are two types of convection, the neutral and forced convection. In the natural convection, forces of gravity are the main factors for dynamics of fluids. However, forced convection enhances the thermal tranfser performance since a collective movement of ensembles of molecules is imposed on the fluid.

In microscales, the dimension of the fluid is insignificant compared to the mean free path of the molecules. In this case the regime is called ballistic.

1.1.3 Energy Transfer by Radiation

Emitting and absorbing electromagnetic radiation of a body at a non-zero temperature can be easily seen from the Stephans-Boltzmann law where the energy absorbed or radiated is directly proportional to the temperature power four. The wavelength λ is the main characteristic length for radiation. In the case where λ is much greater than the characteristic size of the system the radiation can be treated as a simple electrostatic problem and delay effect can be ignored. However, when λ is smaller than the dimensions of the system the electrostatic picture can no longer describe the thermal radiation, since electromagnetic waves cannot be considered as plane waves. In fact, when the characteristic lengths are larger than the wavelength, the far field approximation can be applied. In conclusion, In a material where the wavelength is comparable to the dimension of the system the macroscopic heat transfer is not any more valid and new theories must be considered.

1.2 Introduction to Physics of Phonons

In the present thesis we are focusing on the phonon energy transfer in semiconductors. This section presents the basic theories and laws for describing phonons and their contribution to heat transfer by understanding the laws of lattice dynamics.

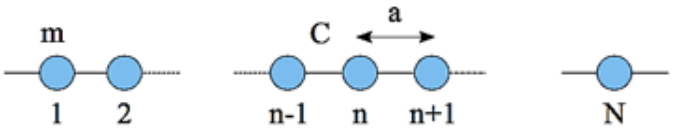

Figure 1.1: Schematic diagram of a monoatomic linear chain that consists of atoms of mass m, separated by a distance a and interacting with a harmonic potential of force constant C

1.2.1 Phonons in a Monoatomic Linear Chain

The vibrations of atoms in a crystal lattice produce phonons, the normal modes of these vibration waves. Phonons are characterized by an angular frequency ω, a wave-vector k and a polarization s.
Consider a monoatomic linear chain that consists of atoms of mass m, force constant C between the atoms, and separated by a distance a. The dynamical equation of the atom when interacting with nearest neighbors is given by:

$$m\frac{d^2u_n(t)}{dt^2} = -C(u_n(t) - u_{n+1}(t)) + C(u_{n-1}(t) - u_n(t)) \tag{1.3}$$

The phonons are considered as plane waves, so the displacement can be written as,

$$u_n(t) = u_0(k)e^{i(\omega t - kna)} \tag{1.4}$$

Substituting equation (1.4) in (1.3), we can get the dispersion relation ω versus the wave vector k in the following relation

$$\omega(k) = 2\sqrt{\frac{C}{m}}|\sin\frac{ka}{2}| \tag{1.5}$$

It is critical to study the dispersion relation in the first Brillouin zone, which is in the interval $[0,2\pi/a[$. In this case, the number of vibrating modes equals the number of degrees of freedom. Figure (1.2) shows the plot of the dispersion relation, for m=10g/mol and C=10N/m, and the group velocity of the phonons which is the derivative of the dispersion relation with respect to the wavevector k.

1.2.2 Phonons in a Diatomic Linear Chain

Figure (1.3) shows a schematic diagram of a diatomic linear chain where two atoms of mass m and M are placed in alternating order on the linear chain. A distance a always separates every neighbor. The interactions between atoms remain identical to the previous case. The Bravais lattice now has a period of $2a$,

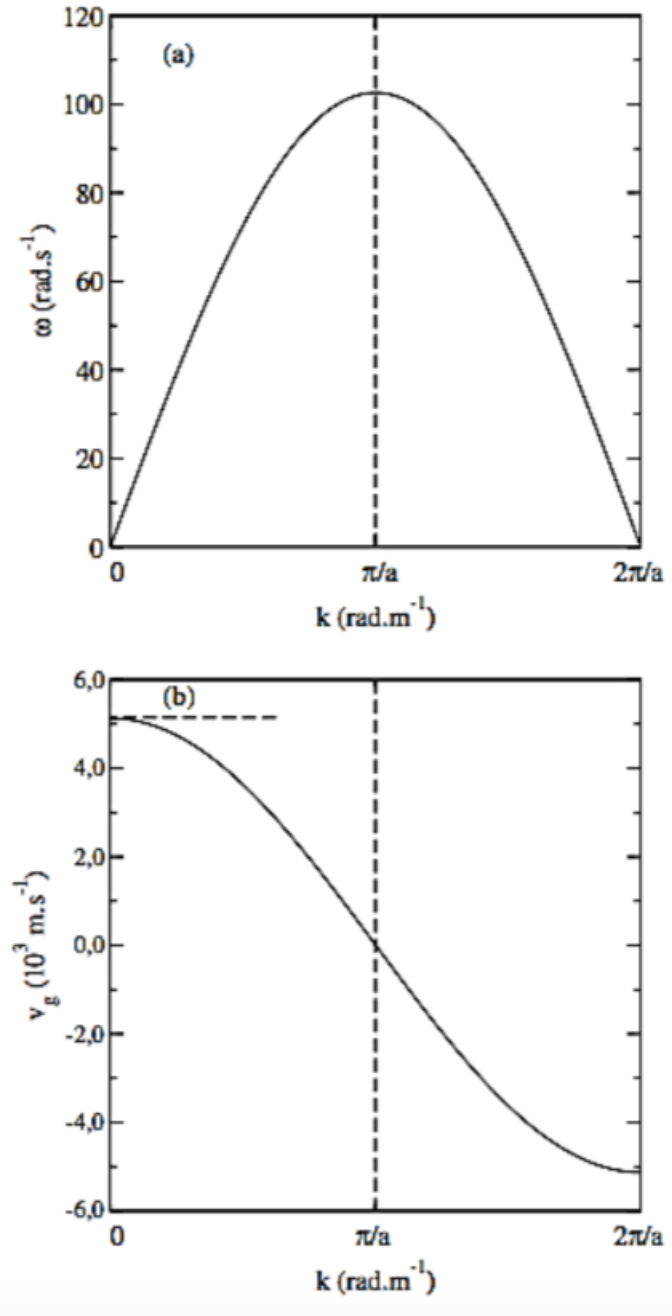

Figure 1.2: a) Dispersion relation for a monatomic linear chain. (b) Group velocity for all phonons of a monatomic linear chain. The dotted horizontal line represents the speed of sound in the material [19].

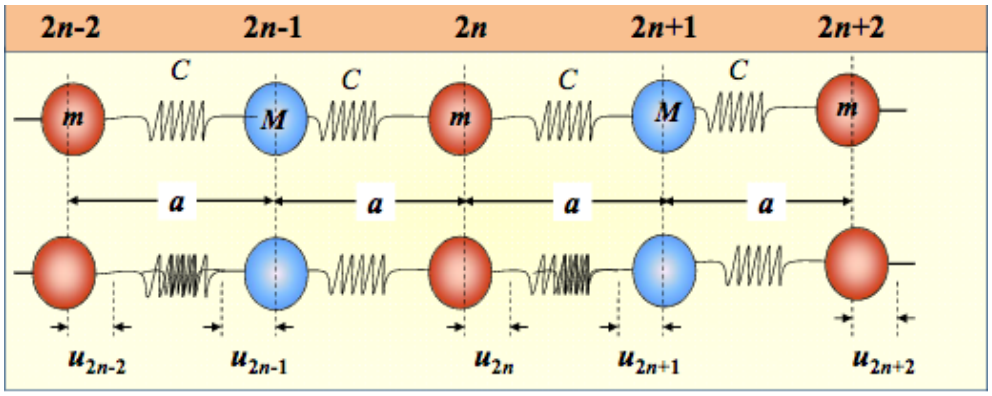

Figure 1.3: Schematic of a diatomic linear chain that consists of atoms of masses m and M, separated by a distance a and interacting with a harmonic potential of force constant C

whereas the first Brillouin zone, which is inversely proportional to the periodicity in the direct space, will be in the interval $[0, \pi/a]$. Hence our interest will be centered on this interval.
The aim is to establish two dynamical equations, one for each atom of the unit cell. We can write:

$$m\frac{d^2u_{2n}(t)}{dt^2} = -C(u_{2n}(t) - u_{2n+1}(t)) + C(u_{2n-1}(t) - u_{2n}(t)) \tag{1.6}$$

$$M\frac{d^2u_{2n+1}(t)}{dt^2} = -C(u_{2n+1}(t) - u_{2n+2}(t)) + C(u_{2n}(t) - u_{2n+1}(t)) \tag{1.7}$$

The displacement for each atom of the primitive cell can be written as progressive planar waves.

$$u_{2n}(t) = u_1(k)e^{i(\omega t - k2na)} \tag{1.8}$$

$$u_{2n+1}(t) = u_1(k)e^{i(\omega t - k(2n+1)a)} \tag{1.9}$$

It is important to note here that the amplitudes of vibration are different for each atom of the unit cell. For each vibration mode, the two atoms do not vibrate in the same manner. Therefore, we are left with a system of two equations with two unknowns.
Substituting equations (1.6 and 1.7) in (1.8 and 1.9), the dispersion relation of phonons which is the angular frequency versus ω as a function of the wavevector k becomes

$$\omega^2 = \frac{C(m+M)}{mM}(1 \pm \sqrt{1 - \frac{4mM\sin^2 ka}{(m+M)^2}}) \tag{1.10}$$

If we consider that the chain consists of N atoms and use cyclic periodic boundary conditions we find the following quantized values for the wavevectors

$$k_n = \frac{2\pi}{Na}n \tag{1.11}$$

Where n is an integer.
The phonons are characterized by a wave packet structure, which allows the definition of their group velocity v_g as the derivative of the angular frequency with respect to the wave vector:

$$v_g(k) = \nabla_k \omega(k) \tag{1.12}$$

The aim is to study the dispersion relation in the first Brillouin zone, precisely in the interval $[0, \pi/2a[$, with n$\in$[0...N -1]. Thus, the number of the vibration modes is equal to the number of degrees of freedom in the system. Figure (1.4) shows the obtained dispersion relations and the associated group velocities with m=10g/mol, M=20g/mol and C=44N/m. The first branch is called the acoustic branch. It is characterized, as in the case of the monatomic chain, by a zero frequency for a zero wave vector. The number of acoustic branches is equal to the dimensionality of the system. Again, in the case of long-wavelengths approximation, the speed of sound is found in the chain, as indicated in Figure(1.4).
The group velocity goes to zero again near the edge/boundary of the Brillouin zone, and therefore it corresponds to a standing wave. The highest branch is called the optical branch. The number of optical branches is normally equal to the total number of degrees of freedom in the primitive cell minus the number of acoustic branches. For these optical branches, the frequency is never zero, even for a zero wave vector. The group velocity goes to zero at the center and near the boundary of the Brillouin zone, and therefore its group velocity is negative, with an absolute value smaller than that of the acoustic branch.
From the figure (1.4) we see that the graph shows two branches, an optical branch and an acoustic branch. The acoustic branch has a zero frequency for wavevector zero, while the optical branch has non-zero frequency even for a zero wavevector. The group velocity of phonons can be obtained from these branches since it is the derivative of the frequency with respect to the wavevector as shown in figure (1.5). For acoustic waves the velocity is higher while for the optical waves the velocity is negative but goes to zero near the boundary and at the center. The amplitude of vibrations will also be different according to different branches. In the acoustic branch, the atoms always vibrate inphase but the amplitude decays near the edge of the BZ which means the energy of this mode is not going to contribute to transfer in the system.

1.2.3 Phonons in a 3D Lattice

After finishing the study of diatomic 1D lattices, we can find by a similar approach the dispersion relation corresponding to a 3D crystal. The dynamical equation

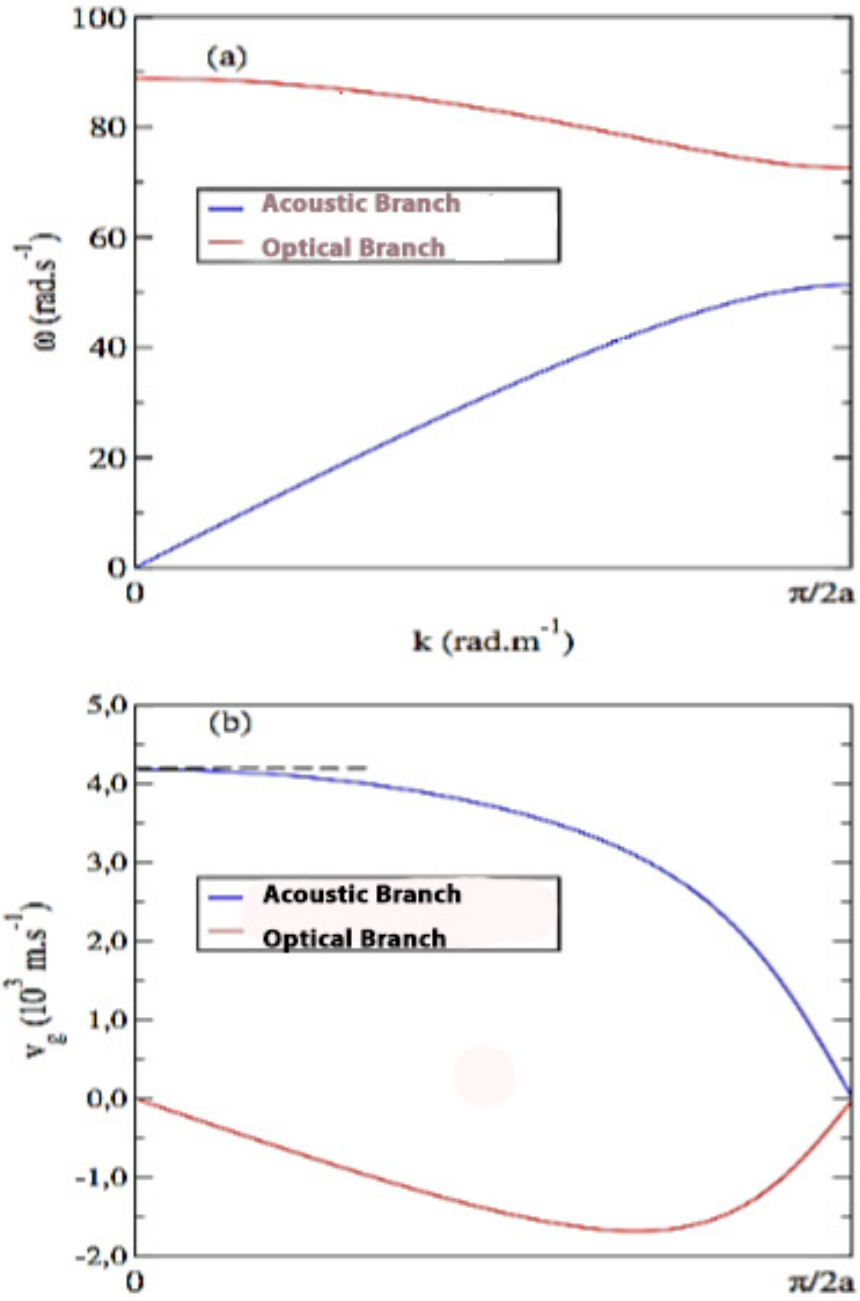

Figure 1.4: (a) The dispersion relations for a diatomic linear chain. (b) The group velocity of all the phonons of a diatomic linear chain. The dotted horizontal line represents the speed of sound in the material [19].

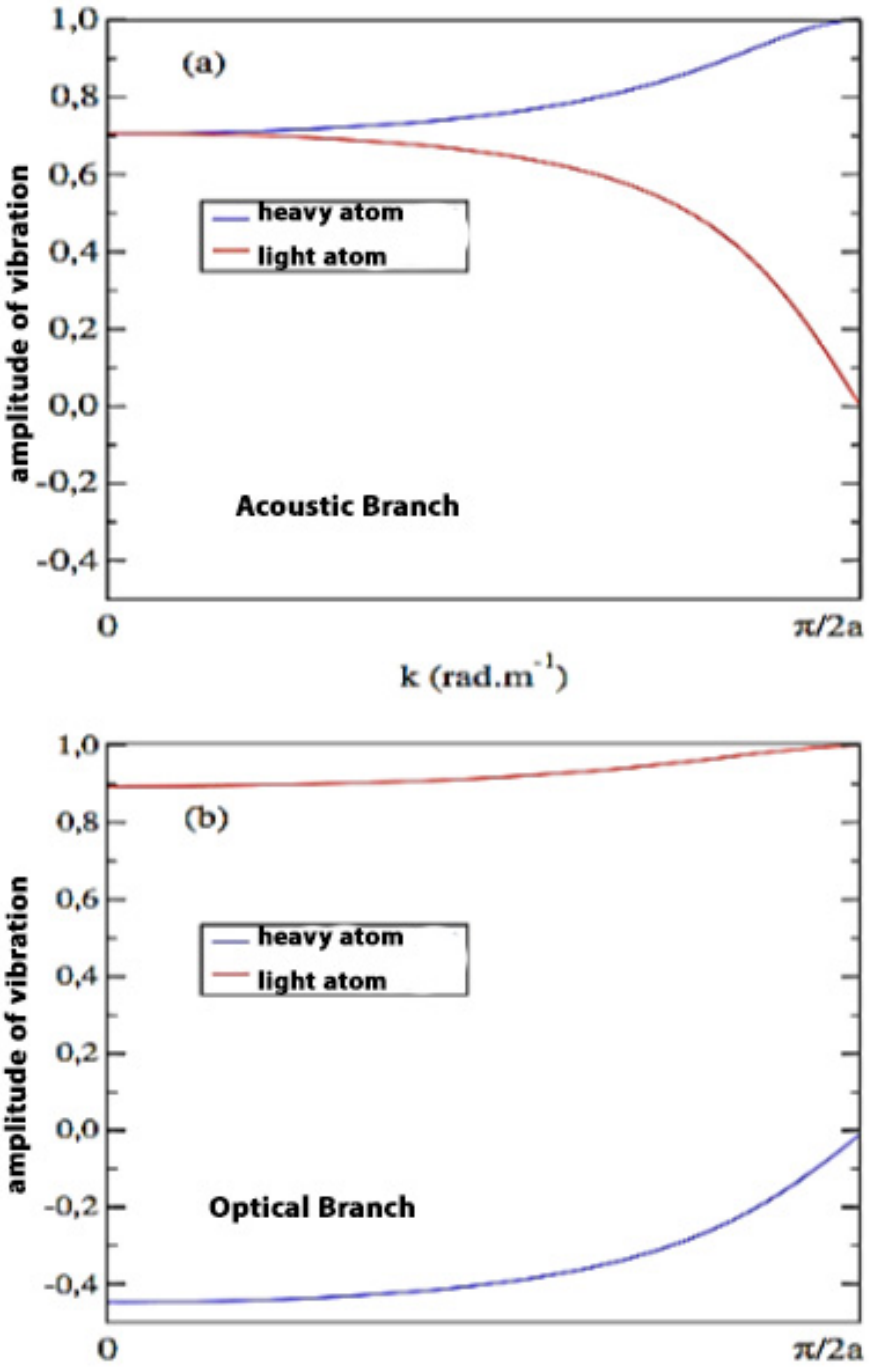

Figure 1.5: (a) Amplitude of vibration of the normal modes for the acoustic branch. (b) Amplitude of vibration of the normal modes for the optical branch [19].

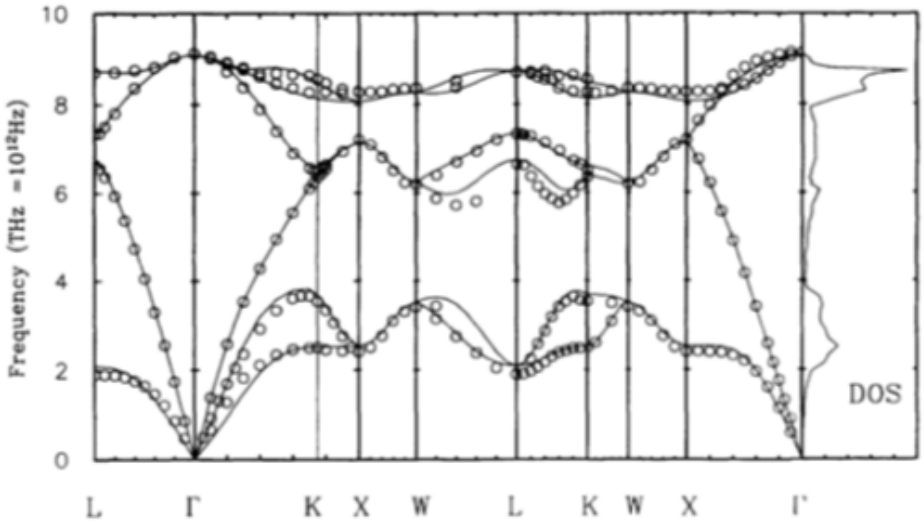

Figure 1.6: The dispersion relations for a bulk Germanium crystal [20].

will be expressed in terms of the potential energy which has the form:

$$E_{tot} = E_0 + \sum_{l,b,\alpha} (\frac{\partial U}{\partial u_l^{b\alpha}})_0 u_l^{b\alpha}(t) + \sum_{l,b,\alpha} \sum_{l',b',\beta'} (\frac{\partial^2 U}{\partial u_l^{b\alpha} \partial u_{l'}^{b'\beta}})_0 u_l^{b\alpha}(t) u_{l'}^{b'\beta}(t) \tag{1.13}$$

Which gives a dynamical equation of the form:

$$m^b \frac{d^2 u_l^{b\alpha}(t)}{dt^2} = -\frac{\partial U}{\partial u_l^{b\alpha}} = -\sum_{l',b',\beta} (\frac{\partial^2 U}{\partial u_l^{b\alpha} \partial u_{l'}^{b'\beta}})_0 u_{l'}^{b'\beta} \tag{1.14}$$

From this dynamical equation the calculation of the dispersion relations in the general case of an arbitrary crystal is obtained and solved numerically. Figure (1.6) shows the plot of the dispersion relation for a bulk Germanium crystal.

1.3 Thermal Transport Models

In the previous sections, the characterization of phonons as the heat carriers which occupy different branches and states and energies was done. From this study we can now proceed to model phonon transport which contributes to heat transport. Thermal transport studies of materials are extremely useful since the world is searching for new materials that can challenge modern device working environment and size. Dissipation of heat in semiconductor materials is very essential to increase the lifetime of a device and to work in harsh environments. The decrease in the size of laptops and smartphones for instance was made possible after overcoming the problem of heat dissipation of materials. On the other hand,

understanding heat transport in materials is useful for choosing different materials for different applications. Low thermal conductivity materials which also have high electrical conductivity can be used as thermoelectric devices. In the following section we will describe the theoretical models for calculating thermal conductivity and heat capacity in a given material.

1.3.1 Callaway's Model for Thermal Conductivity

For the study of thermal conductivity, we consider the different directions of propagation of waves in a crystal. Usually, each high symmetry direction affects the overall lattice thermal conductivity of the crystal. The phonon heat current $\mathbf{j}$ along any direction in any crystal can be considered as the sum of individual vector components $\mathbf{j}_{hkl}$ directed along the high- symmetry directions [h,k,l] of the crystal. Thus, we may write

$$\mathbf{j} = \sum_{[h,k,l]} \mathbf{j}_{hkl} \tag{1.15}$$

where the summation runs over all the high-symmetry directions of the crystal. On the other hand, the individual component $\mathbf{j}_{hkl}$ of the total heat current $\mathbf{j}$ is defined as the sum over all states k_{hkl} of the number of phonons with a given frequency that are incident per unit time parallel to the high symmetry direction [h,k,l], times the phonon energy $\hbar\omega(k_{hkl})$. This can be expressed as

$$\mathbf{j}_{hkl} = \sum_{[h,k,l]} \hbar\omega(k_{hkl}) N(k_{hkl}).\mathbf{v}_{hkl} \tag{1.16}$$

Here, $\mathbf{v}_{hkl}$ is the phonon velocity in the high symmetry direction [h,k,l], and $N(k_{hkl})$ is the phonon distribution in the state k_{hkl}, defined as the sum of the phonon distribution at equilibrium $\bar{N}(k_{hkl})$ and the deviation of the phonon distribution from equilibrium $\widetilde{N}(k_{hkl})$ in the state k_{hkl}. Typically, in an infinite crystal, the change in the phonon distribution is due to the combined effects of temperature gradient together with phonon collisions with each other and defects. In the steady state regime, the total rate of change in the phonon distribution must vanish. Thus, Boltzmann equation, which describes this total rate of change in the phonon distribution, takes the form

$$-\mathbf{v}_{hkl}.\nabla N(k_{hkl}) + \frac{\partial N(k_{hkl})}{\partial t} = 0 \tag{1.17}$$

The usual way to solve equation (1.17) is to approximate its second term by $\frac{\partial N(k_{hkl})}{\partial t} = \frac{\bar{N}(k_{hkl}) - N(k_{hkl})}{\tau(k_{hkl})}$. With this approximation, it is assumed that in the absence of a temperature gradient, any deviation from equilibrium in the state k_{hkl} damps out rapidly in a time $\tau(k_{hkl})$. This approximation is valid in some circumstances, but it generally ignores the difference between the physical nature of the normal

processes, which tend to displace the phonon distribution by a small vector $\mathbf{u}$ in the direction of the heat current, and the nature of the resistive processes, which tend to restore it back to its equilibrium value. Although the normal processes do not contribute to the thermal resistance, they must be taken into account when solving Boltzmann equation, because they cause the deviation of the phonon distribution function in a direction opposite to the resistance direction. The disregard of this effect often leads to inaccurate estimation of the magnitude of κ. Therefore, a more accurate approximation to the second term in equation (1.17) would be given by

$$\frac{\partial N(k_{hkl})}{\partial t} = \frac{N_{\mathbf{u}}(k_{hkl}) - N(k_{hkl})}{\tau_N(k_{hkl})} + \frac{\bar{N}(k_{hkl}) - N(k_{hkl})}{\tau_R(k_{hkl})} \tag{1.18}$$

Where $N_{\mathbf{u}}(k_{hkl})$ is the displaced phonon distribution, which is stationary in the state k_{hkl} for the normal processes, and $\tau_{N(R)}(k_{hkl})$ the relaxation time associated with normal (resistive) processes. In the case of an infinite crystal, the spatial dependence of the phonon distribution function can be ignored and equation (1.17) reduces to

$$-v_{z,hkl}\frac{d\bar{N}(k_{hkl})}{dT}.\frac{\partial T}{\partial z} + \frac{\partial N}{\partial t} = 0 \tag{1.19}$$

In equation (1.19), it is assumed that the temperature gradient is directed along the z direction and is too weak to alter the deviation of the phonon distribution. By using equation (1.18) in equation (1.19) and following Callaways mathematical arrangements [23,24], the individual component of the total phonon heat current takes the form

$$\mathbf{j}_{hkl} = -\sum_{k_{hkl}} \tau(k_{hkl}))\mathbf{v}_{hkl}.\nabla T_{hkl} \times \frac{\hbar\omega(k_{hkl})}{k_b T^2} \frac{e^{\frac{\hbar\omega(k_{hkl})}{k_b T}}}{(e^{\frac{\hbar\omega(k_{hkl})}{k_b T}}-1)^2}\mathbf{v}_{hkl} \tag{1.20}$$

where $\nabla T_{hkl} = \nabla T cos\psi_{hkl}$ (the component of the temperature gradient aligned parallel to the high symmetry direction[h,k,l], with ψ_{hkl} being the angle between the crystallographic direction along which the temperature gradient is directed and the high-symmetry direction [h,k,l]. In equation (1.20), $\tau(k_{hkl})$ is the total relaxation time defined as $\tau(k_{hkl}) = \tau_C(k_{hkl})[1 + \frac{\beta_{hkl}}{\tau_N(k_{hkl})}]$, with $\tau_C(k_{hkl})$ being a combined relaxation time for the state k_{hkl} defined as $\frac{1}{\tau_C(k_{hkl})} = \frac{1}{\tau_N(k_{hkl})} + \frac{1}{\tau_R(k_{hkl})}$ and β_{hkl} a parameter with the dimension for a relaxation time given by

$$\beta_{hkl} = \frac{\int_0^{\theta_{D,hkl}/T} dx \frac{x^4 e^x}{(e^x-1)^2} \frac{\tau_C(k_{hkl})}{\tau_N(k_{hkl})}}{\int_0^{\theta_{D,hkl}/T} dx \frac{x^4 e^x}{(e^x-1)^2} \frac{1}{\tau_N(k_{hkl})}(1 - \frac{\tau_C(k_{hkl})}{\tau_N(k_{hkl})})} \tag{1.21}$$

Where $x = \frac{\hbar\omega(k_{hkl})}{k_B T}$ is a dimensionless parameter. Thus, the thermal conductivity along the high-symmetry direction [h,k,l] can be written as

$$\kappa = -\frac{\mathbf{j}_{hkl}}{\nabla T} = \sum_{k_{hkl}} \sum_j \tau_j(k_{hkl}) \bar{v}^2_{j,hkl} \frac{\hbar\omega_j(k_{hkl})}{k_B T^2} \times \frac{e^{\frac{\hbar\omega_j(k_{hkl})}{k_b T}}}{(e^{\frac{\hbar\omega_j(k_{hkl})}{k_b T}}-1)^2} cos\psi_{hkl} \tag{1.22}$$

where the subscript j denotes the phonon polarization and $\bar{v}_{j,hkl}$ is a temperature-dependent phonon group velocity averaged over all k_{hkl} states. By combining this equation with equation (1.15), one can readily find that the thermal conductivity in an infinite crystal along a well-defined crystallographic direction takes the form

$$\kappa = \sum_{[hkl]} \sum_{k_{hkl}} \sum_{j} \tau_j(k_{hkl}) \bar{v}^2_{j,hkl} \frac{\hbar\omega_j(k_{hkl})}{k_B T^2} \times \frac{e^{\frac{\hbar\omega_j(k_{hkl})}{k_b T}}}{(e^{\frac{\hbar\omega_j(k_{hkl})}{k_b T}} - 1)^2} cos\psi_{hkl} \tag{1.23}$$

and the average thermal conductivity of the same crystal is

$$\bar{\kappa} = \frac{1}{m} \sum_{[hkl]} \sum_{k_{hkl}} \sum_{j} \tau_j(k_{hkl}) \bar{v}^2_{j,hkl} \frac{\hbar\omega_j(k_{hkl})}{k_B T^2} \times \frac{e^{\frac{\hbar\omega_j(k_{hkl})}{k_b T}}}{(e^{\frac{\hbar\omega_j(k_{hkl})}{k_b T}} - 1)^2} \tag{1.24}$$

where m is the number of high-symmetry directions in the crystal structure under consideration. We note here that the number of high-symmetry directions in a given crystalline structure equals the number of independent elastic constants [25].The major importance of equations (1.23) and (1.24) stems in that they can be used to describe κ either for a specific surface orientation or as an average over all crystallographic directions, with taking into account the various intrinsic phonon processes that may influence the heat transport mechanism [23, 24].

1.3.2 Debye Model for Heat Capacity

In fact, it was known that at low temperatures most materials have a heat capacity that is proportional to T^3. In 1912 Peter Debye discovered how to better treat the quantum mechanics of the oscillations of atoms, and managed to explain the T^3 dependance of the specific heat. Debye realized that the oscillation of atoms is the same thing as sound, and sound is a wave, so it should be quantized the same way as Planck had quantized light waves in 1900 [26].
We will consider waves with periodic or Bornvon Karman boundary conditions. It is easiest to describe this first in one dimension i.e. in infinite crytals. Here, instead of having a one-dimensional sample of length L with actual ends, we imagine that the two ends are connected together making the sample into a circle. The periodic boundary condition means that, any wave in this sample e^{ikr} is required to have the same value for a position r as it has for r+L (we have gone all the way around the circle). This then restricts the possible values of k to be

$$k = \frac{2\pi n}{L} \tag{1.25}$$

for n an integer. If we are ever required to sum over all possible values of k, for large enough L we can replace the sum with an integral obtaining

$$\sum_{k} \rightarrow \frac{L}{2\pi} \int_{-\infty}^{\infty} dk \tag{1.26}$$

A way to understand this mapping is to note that the spacing between allowed points in k space is $2\pi/\mathrm{L}$, so the integral $\int dk$ by a sum over k points times the spacing between the points.
In three dimensions, the story is extremely similar. For a sample of size L^3, we identify opposite ends of the sample (wrapping the sample up into a hypertorus!) so that if you go a distance L in the x, y or z direction, you get back to where you started. As a result, our k values can only take values

$$\mathbf{k} = \frac{2\pi}{L}(n_1, n_2, n_3) \tag{1.27}$$

for integer values of n_i, so here each k point now occupies a volume of $(2\pi/\mathrm{L})^3$. Because of this discretization of values of k, whenever we have a sum over all possible k values we obtain

$$\sum_k \rightarrow \frac{L^3}{(2\pi)^3}\int_{-\infty}^{\infty} \mathbf{dk} \tag{1.28}$$

Debye decided that the oscillation modes of a solid were waves with frequencies $\omega(\mathbf{k}) = v|\mathbf{k}|$ with v the sound velocity and for each $\mathbf{k}$ there should be three possible oscillation modes, one for each direction of motion. After doing the calculations Debye found the average energy to be

$$\langle E\rangle = \int_0^{\infty} d\omega g(\omega)(\hbar\omega)(n_B(\beta\hbar\omega) + \frac{1}{2}) \tag{1.29}$$

Where $\beta = 1/k_B T$ and n_B is the Bose factor such that $n_B(x) = 1/(e^x - 1)$ and $\mathrm{g}(\omega)$ is the density of state give by

$$g(\omega) = N\frac{9\omega^2}{\omega_d^3} \tag{1.30}$$

Where

$$\omega_d^3 = 6\pi^2 n v^3 \tag{1.31}$$

This frequency will be known as the Debye frequency and n is the density of the atoms give by $nL^3 = N$.The meaning of the density of states here is that the total number of oscillation modes with frequencies between $\omega$and $\omega + d\omega$ is given by $g(\omega)d\omega$. We are concerned with heat capacity which is partial derivative of energy with respect to time

$$C = \frac{\partial\langle E\rangle}{\partial T} = Nk_B\frac{(k_B T)^3}{(\hbar\omega)^3}\frac{12\pi^4}{5} \sim T^3 \tag{1.32}$$

Unfortunately, now Debye has a problem. In the expression just derived, the heat capacity is proportional to T^3 up to arbitrarily high temperature. We know

however, that the heat capacity should level off to $3k_BN$ at high T. Debye guessed (correctly) that really there should be only as many modes as there are degrees of freedom in the system. To fix this problem, Debye decided to not consider sound waves above some maximum frequency ω_{cutoff}, with this frequency chosen such that there are exactly 3N sound wave modes in the system (three dimensions of motion times N particles). We thus define ω_{cutoff} via

$$3N = \int_0^{\omega_{cutoff}} d\omega g(\omega) \tag{1.33}$$

Following the same procedure we did befor we find the heat capacity at the limit of high temperature to be $3k_BN$ [26].
From the knowledge of the material thermal conductivity and specific heat, the material heat diffusivity can be derived from equation (1.2).

1.3.3 Phonon Heat Transport Approaches

Three main approaches are known in the study of phonon transport. The first is the study of Boltzmanns transport equation whose solution enters the expression of the thermal conductivity when thermal energy transfer by particle-like carriers is assumed. The Boltzmann equation is considered the classical approach to the heat transfer where elasticity theory is involved to obtain the strain and stress tensors from which we deduce the elastic waves equation and deduce the dispersion relation of the material. The dispersion relation allows us to calculate the frequency of phonons having different wave-vectors with the frequency and dispersion curve of the material, we identify the normal modes and then many thermal properties can be obtained such as specific heat. Next the phonons interactions are studied by analyzing their relaxation times. These phonons interact by creation and annihilation processes while maintaining a conservation of energy. These anharmonic interactions between the lattice normal modes can occur via non-resistive normal processes or resistive Umklapp processes. The main difference between these processes is that in the case of anharmonic interactions via normal processes one must consider momentum conservation, while momentum conservation exists in Umklapp processes. Other phonon processes include boundary interactions and point defect phonons interactions. These processes are similar to Umklapp phonon processes. The major similarity is that all these phonon processes affect the momenta of the involved phonons. That is why we consider resistive phonon processes to include Umklapp phonon processes rate and those of point defect and boundary interactions to give the overall resistive scattering rate. The resistive phonon interaction processes are the contributors to the shifting of phonon heat current to zero. These mechanisms, along with their relation to the thermalization and resistance to the heat flow, are described by several theories. This approach works well at high energies. However, at low energies, the quantum theory is involved. Studying phonons in the quantum

mechanical point of view was discussed in the ab-initio study. Ab-initio uses quantum mechanical approach by solving Schrodinger equation, with some weak approximations, to find force constants and consequently finds the thermal properties of the crystals.The last approach to tackle the phonon transfer problem is the molecular dynamic method in which it uses Newton's laws as its starting point, so by calculating position and velocity other properties can be found. In this case phonons in solids are considered as a box of particles, similar to the study of a gas. Then by simulation techniques, such as the Monte Carlo study, the dynamics of phonons and their mode of transfer is predicted depending on different elastic and thermal properties of the material. A computer simulation is used to numerically solve the equations of motion for obtaining the vibrational modes of a material. However, MD is an extremely lengthy process. It considers interactions within a material atom by atom, and therefore the simulations are too long and sometimes do not provide correct results due to lack of theoretical studies and considerations of heat transfer physical laws.

1.4 Experimental Measurement of Heat Properties

On the other hand, several experimental methods are used to measure the heat transfer in materials. These include photoacoustic microscopy, where a sample is enclosed with a gas in an isolated volume and pressure variation is measured to obtain a thermal wave image. A well-known method is the mirage effect method. In this case the gradient of the index of refraction of the air in contact with the sample is detected by a probe beam. [8–10] Infrared detection is also a well know method of measurement of heat emitted by a sample.

1.4.1 Thesis problem

In this dissertation, we intend to investigate the physics of heat transport in silicon carbide substrate bombard by H^+ ions. These bombardment are expected to generate strains, and consequently elastic fields, which may scatter the phonons. Hence, the work outlined in this thesis will describe the effect of elastic field on phonon scattering and heat transport.

Chapter 2

Theory of the Mirage Effect

The mirage effect is based on a theory, which can be used to obtain the thermal properties of the measured sample. This theory is presented below.

2.1 Thermal waves

The total temperature field T, as a function of position $\mathbf{x}$ and time t, is described by the general heat conduction equation [8].

$$\rho c_p \frac{\partial T(\mathbf{x},t)}{\partial t} = \nabla.(\kappa \nabla T(\mathbf{x},t)) \tag{2.1}$$

Where ρ is the density, c_p is the specific heat at constant pressure and κ is the thermal conductivity. For a steady state regime where the partial derivative of temperature with respect to time is zero, the heat equation is independent of material properties and will only depend on the geometry of the body. Hence equation (2.1) will be simplified to Laplace equation. In general, the density, heat capacity and thermal conductivity are important parameters since they describe heat transfer inside the material.
In the case of composite samples κ will be a function of the position i,e, $\kappa = \kappa(\mathbf{x})$ with constant ρ and c_p. We can then obtain a solution to the equation (2.1) [8]. For a homogeneous isotropic solid whose thermal conductivity is independent of position, equation (2.1) becomes

$$\rho c_p \frac{\partial T}{\partial t} = \kappa \nabla^2 T \tag{2.2}$$

Another important derived thermal property is the thermal diffusivity,

$$\alpha = \frac{\kappa}{\rho c_p} \tag{2.3}$$

where α is the diffusivity of the substance. The quantity is called by Clerk Maxwell as the Thermometric conductivity since it measures the change of temperature, which should be produced in a unit volume of the substance, by the

quantity of heat which flows in a unit time through a unit area of a layer of the substance of a unit thickness with a unit difference of temperature between its faces [8]. The thermal diffusivity, besides being a derivable quantity, is an important thermal parameter, and for homogeneous materials it will replace the two thermal parameters of equation (2.2). We can solve this equation then for thermal diffusivity instead of dealing with two thermal properties to solve the heat equation. Microcracks, delamination, and impurities are thermal barriers that give non uniform diffusivity values. Thus the thermal diffusivity measurement can be used as an efficient structural characterization technique [9].
This equation is known as heat equation where α is the thermal diffusivity of the material. In our experiment a heating source is used to heat the sample so we add to the heat equation a term associated to the heat source.

$$\nabla^2 T(\mathbf{x},t) - \frac{\rho c_p}{\kappa}\frac{\partial T(\mathbf{x},t)}{\partial t} = -\frac{A(\mathbf{x},t)}{\kappa} \tag{2.4}$$

Here $A(\mathbf{x},t)$ is the total amount of heat deposited per unit time per unit volume by the heat source. If we have a periodic source of heat with angular frequency ω, A will have the following form,

$$A(\mathbf{x},t) = A(\mathbf{x})e^{-i\omega t} \tag{2.5}$$

If the temperature also has the same form as (2.5), equation (2.4) will be

$$\kappa\nabla^2 T(\mathbf{x}) + \kappa q^2 T(\mathbf{x}) = -A(\mathbf{x}) \tag{2.6}$$

where q is the thermal complex wave number given by [10]

$$q = \sqrt{\frac{i\omega\rho c_P}{\kappa}} = (1+i)\sqrt{\frac{\omega\rho c_p}{2\kappa}} \tag{2.7}$$

The appearance of "thermal waves" comes from equation (2.4) due to the equivalence with Helmhotz equation for wave motion, which results in a wave-like solution [8,10]. The wave number q has real and imaginary parts, so the solution of the equation should fall to 1/e after covering a distance called the "thermal diffusion length"μ .

$$\mu = \sqrt{\frac{2\kappa}{\omega\rho c_P}} \tag{2.8}$$

If we have a heat source applied to a material with variable frequency pulses, the physical intuition tells us that if we increase the frequency the heat will reach smaller distance in the material. This is because the material doesn$'$t have enough time to absorb heat, and it will dissipate heat directly. The reversed mechanism also true. On the other hand, the thermal diffusion length is inversely proportion to the square root of the frequency, so the penetration depth of thermal waves

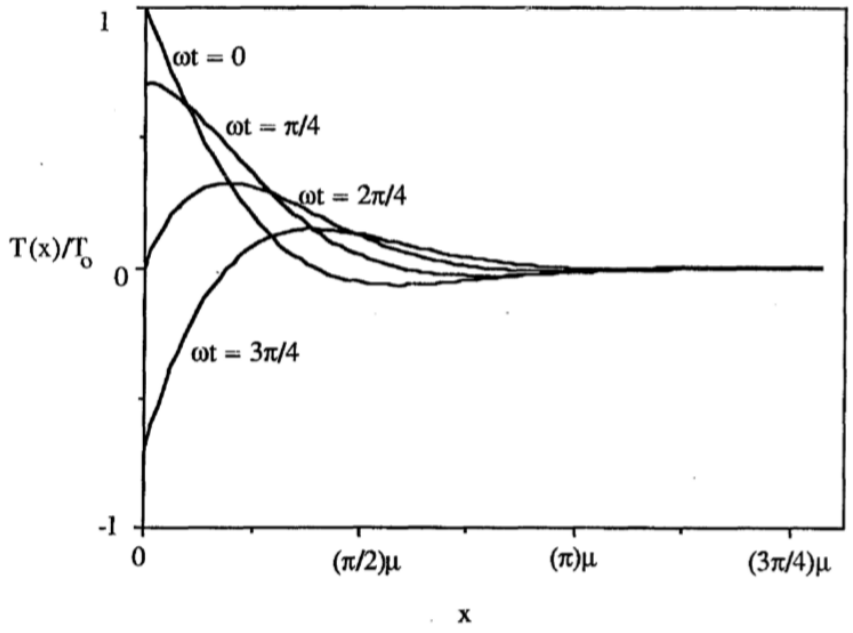

Figure 2.1: Spatial distribution of the time-independent temperature for a 1-d heat flow [9]

may be varied according to the frequency where it usually varies from the order of microns to millimeter according to the material type and frequency. This short penetration depth makes the mirage effect technique a useful tool for imaging near surface features. The wavelength of a thermal wave is

$$\lambda_{thermal} = 2\pi\mu \tag{2.9}$$

The amplitude of the thermal wave decreases by a factor of $e^{-2\pi} \approx 1/500$ after traveling one wavelength. This means that the experiment involving scattering of thermal waves must lunch, scatter, and receive the wave in a total propagation distance not much larger than a wavelength. For a 1D case, where the reference is taken at x=0, using equation (2.6) T is found to be

$$T(x,t) = T_0 e^{i(qx-wt)} \tag{2.10}$$

where T_0 is the amplitude of the thermal wave as $x \to 0$. A plot to the real part of $T(x,t)/T_0$ versus distance x in terms of thermal diffusion length is shown in figure (2.1).

2.2 Theoretical description of mirage effect experiment

Mirage-effect experiment is used to measure the thermal properties of a uniform material such as substrate of metal or semiconductor, thin films, and superlattices. Determination of the thermal wavelength in equation (2.9) as a function of frequency is useful since the slope of the plot of that wavelength versus the reciprocal of the inverse of the square root of the frequency is a function of the thermal diffusivity ,α, of the material. The derivation of the theory of mirage effect explains exactly how this is accomplished. The main concept of the mirage effect experiment is the detection of thermal waves in solids where the temperature distribution creates a temperature gradient which leads to an index of refraction gradient in the gas above the sample which is detected by a second laser beam called probe beam directed along the surface of the sample near the heating spot which is generating thermal waves. In addition, the heat capacity of the air is so small compared to that of the solid, so the temperature distribution in the air very close to the surface of the sample is determined by the temperature distribution in the solid. Then, the deflection of the probe beam by a refractive index gradient produces a measured signal. However, the deflection angle is very small, typically less than Millie-radiant, so that the path of the probe beam is considered to be a straight line across the surface. [10]
The formula of the deflection of the mirage probe is found to be [11–13]

$$M = -\int \frac{1}{n}\frac{dn}{dT}\nabla T(\mathbf{r}) \times d\mathbf{r} \tag{2.11}$$

Where M is the vector angular deflection. This formula expresses the angle of deflection in terms of an integral of the fractional change in the index of refraction, and the temperature in the air. Since the expected temperature variation are quite small, it is reasonable to assume that the ratio $(dn/dT)/n$ will be essentially constant over the path. Typically, dn/dT is $10^{-4}/^{\circ}C$ for liquids and $10^{-5}/^{\circ}C$ for solids [12]. Moreover, the angular deflection is small, so the direction of the beam path, d$\mathbf{r}$, can be taken to be constant, say in the y-direction, so the deflection can be written to a high degree of accuracy as,

$$M = -\frac{1}{n}\frac{dn}{dT}\nabla \bar{T}(x,z) \times \hat{y} \tag{2.12}$$

where the bar indicates an average over the y-coordinate. The average reduces the problem to a two dimensional one. The main important point left is to find the temperature distribution in the material according to its type which will help us in the calculation of the vector angular deflection.

2.2.1 Bulk Materials

The temperature which appears in equation (2.12) is the temperature for the medium above the sample which is usually air, so the thermal wave problem that must be solved is one with two media: The first medium is the gas above the sample which will be denoted by g as a subscript in the studied parameters, the second medium is the sample and will be denoted by s as a subscript. The gas will be taken to occupy the region z<0 and the sample region z≥0. The wave equation that must be solved can then be written as

$$\nabla.[\kappa_g \nabla \bar{T}_g(x,z)] + \kappa_g q_g^2 \bar{T}_g(x,z) = 0; z < 0, (gas) \tag{2.13}$$

and

$$\nabla.[\kappa_s \nabla \bar{T}_s(x,z)] + \kappa_s q_s^2 \bar{T}_s(x,z) = -\delta(x)\delta(z); z \geq 0, (solid) \tag{2.14}$$

where we have assumed that the heating beam is a point source of unit strength at x=0 and z=0. These equations are perhaps most easily solved by writing the temperature,$\bar{T}(x,z)$, as a fourier transform in x,

$$\bar{T}(x,z) = \int_{-\infty}^{\infty} dk e^{ikx} t(k,z) \tag{2.15}$$

equations (2.13) and (2.14) then become,

$$\frac{\partial}{\partial z}[\kappa_g \frac{\partial}{\partial z} t_g(k,z)] + \kappa_g k_g^2 t_g(k,z) = 0 \tag{2.16}$$

and

$$\frac{\partial}{\partial z}[\kappa_s \frac{\partial}{\partial z} t_s(k,z)] + \kappa_s k_s^2 t_s(k,z) = \frac{-1}{2\pi}\delta(z) \tag{2.17}$$

where

$$k_g = (q_g^2 - k^2)^{1/2} \tag{2.18}$$

and

$$k_s = (q_s^2 - k^2)^{1/2} \tag{2.19}$$

Since the only source is located at z=0, the thermal waves must propagate away from that plane, i.e., in the negative z-direction for z<0, and in the positive z-direction for z>0. Thus, they can be written as

$$t_g(k,z) = C_g e^{-ik_g z} \tag{2.20}$$

and

$$t_s(k,z) = C_s e^{ik_s z} \tag{2.21}$$

The boundary conditions that must be applied to these waves are the temperature continuity across the plane, z=0, and the heat flux discontinuity which corresponds to the source strength in equation (2.17) on the same plane,

$$C_g = C_s \tag{2.22}$$

$$i\kappa_s k_s C_s + i\kappa_g k_g C_g = -\frac{1}{2\pi} \tag{2.23}$$

These equations can be solved for the constant C_g,

$$C_g = \frac{i}{2\pi(\kappa_s k_s + \kappa_g k_g)} \tag{2.24}$$

The mirage deflection signal can now be obtained by combining equations (2.12), (2.15), (2.20), (2.21), and (2.24).

$$M = \frac{i}{2\pi}\frac{1}{n}\frac{dn}{dT}\hat{y} \times \nabla \int_{-\infty}^{\infty} \frac{e^{i(kx-k_g z)}}{\kappa_s k_s + \kappa_g k_g} \tag{2.25}$$

The equation (2.25) describes the signal produced by an infinitesimally narrow probe beam scanning the region of a point heating beam. However, in experimental work, both the probe beam and heating beam radii are significant which affects the formula of the deflection, so we should produce a theoretical expression that can be compared with data from real experiments in which both of these beams have finite radii. Consequently, we assume that both beams have Gaussian profiles with R_1 and R_2 representing the radii of the heating beam and probe beam, respectively. The heating beam will be assumed to be centered at the origin, and the probe beam centered at a distance, x, horizontally away from the origin and a height, h, above the surface as in figures (2.2) and (2.3). Equation (2.25) contains only simple exponential functions of$x$ and z, these Gaussian averages can be performed analytically, yielding final expressions for the normal(z-direction) and tangential(x-direction) deflections of the probe beam,

$$M_{norm} = \frac{-1}{\pi}\frac{1}{n}\frac{dn}{dT}e^{-\frac{q_g^2 R_2^2}{4}} \int_0^{\infty} dk \frac{k_g cos(kx) e^{ik_g h} e^{-k^2 R_1^2/4}}{\kappa_s k_s + \kappa_g k_g} \tag{2.26}$$

and

$$M_{tan} = \frac{-i}{\pi}\frac{1}{n}\frac{dn}{dT}e^{-\frac{q_g^2 R_2^2}{4}} \int_0^{\infty} dk \frac{k sin(kx) e^{ik_g h} e^{-k^2 R_1^2/4}}{\kappa_s k_s + \kappa_g k_g} \tag{2.27}$$

In these expressions we have used the symmetry in the integrand to express the deflections as integrals from zero to infinity with trigonometric functions in x, rather than from minus infinity to infinity with exponential functions. It′s clear from equations (2.26) and (2.27) that the normal deflection as in figure (2.5) is an even function of the horizontal offset, x, between the heating and probe beams, and that the tangential deflection as in figure (2.4) is an odd function of the offset. The technique for measuring the thermal diffusivity involves measuring M_{tan} as a function of the offset distance, x, in the limit of very small probe beam height, h [14–16]. The dependence of M_{tan} on the thermal diffusivity of the sample is through the quantity k_s which appears in the denominator of the integrand and which was defined in equation (2.19). Except for the overall phase factor involving

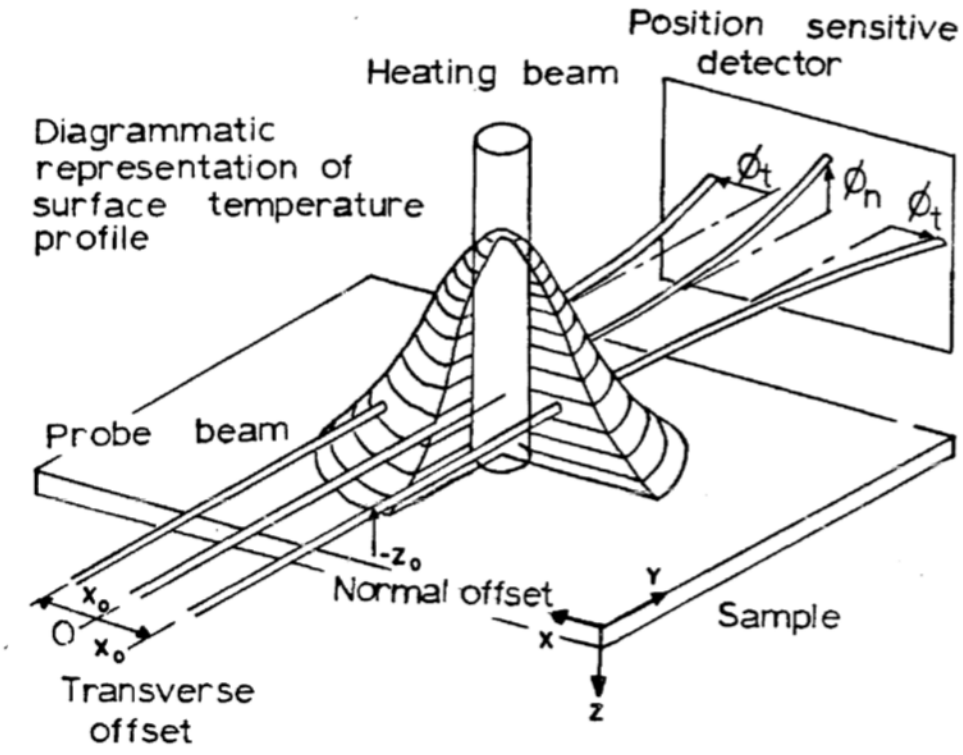

Figure 2.2: mirage-effect geometry [9]

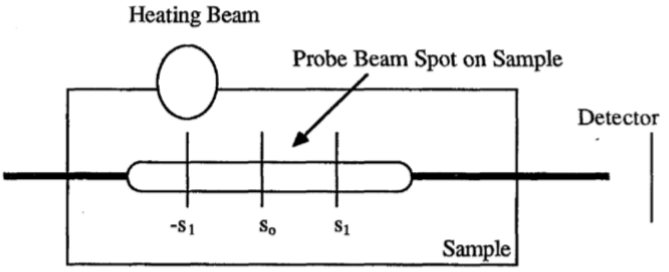

Figure 2.3: Top view of the sample which shows the probe beam spot and several positions on the probe beam axis. In the diagram, the heating beam scans the probe beam at the position $-s_1$ [9].

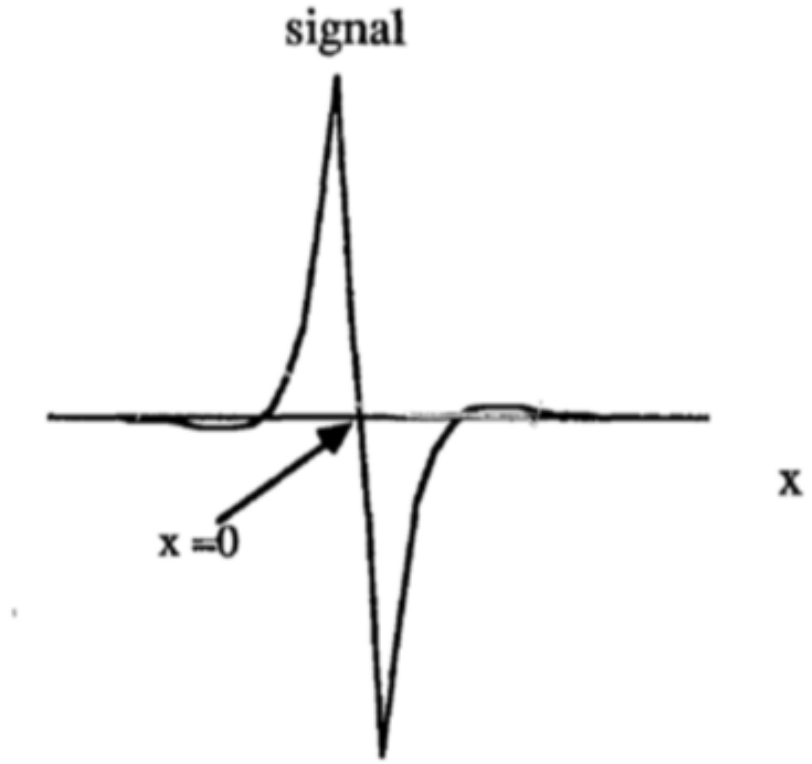

Figure 2.4: The real part of the transverse deflection versus the offset distance x [9]

the probe beam radius, R_2, its dependence on k_g, at least for small values of h, is quite weak. Plots of the real part of the function versus the offset, x, for a small value of R_1 are given in figure (2.6). The antisymmetric of the function is quite apparent as is the fact that it represents a very heavily damped wave. The two points at which this plot of the real part of M_{tan} heavily damped wave. The two points at with this plot of the real part of M_{tan} first goes to zero on either side of the central zero are of particular interest. Since the real part of the function vanishes there, the function is purely imaginary, corresponding to values of the phase $\pm\pi/2$. A numerical analysis shows that the distance x_0, between the two ninety degree phase points on either side of the origin is given by

$$x_0 = d + \sqrt{1.4\pi\alpha/f} \tag{2.28}$$

where d is a distance of the order of the heating beam diameter and where f is the frequency ($f = \omega/2\pi$). Thus, a plot of x_0 versus the reciprocal of the square root of the frequency should have a slope given by $\sqrt{1.4\pi\alpha}$ and an intercept which is dependent on the size of the heating beam. A theoretical and experimental plot of this type for chromium is shown in figure (2.7). It is important, when

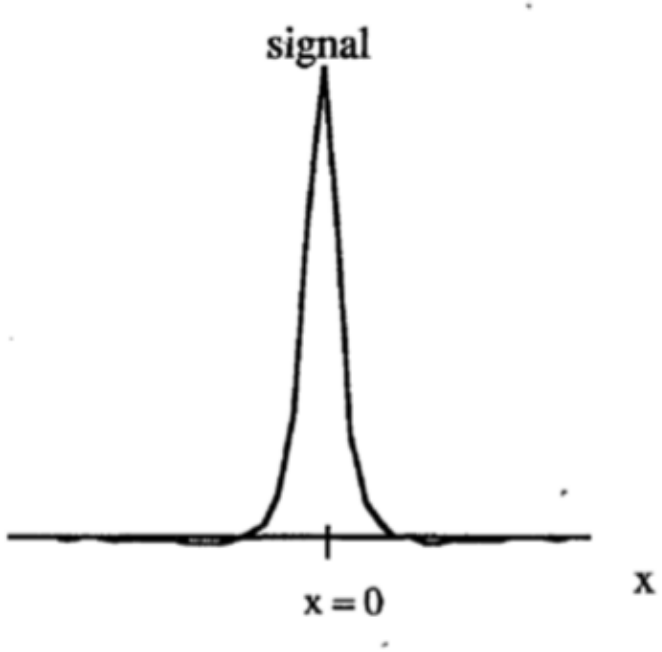

Figure 2.5: The real part of the normal deflection versus the offset distance x [9]

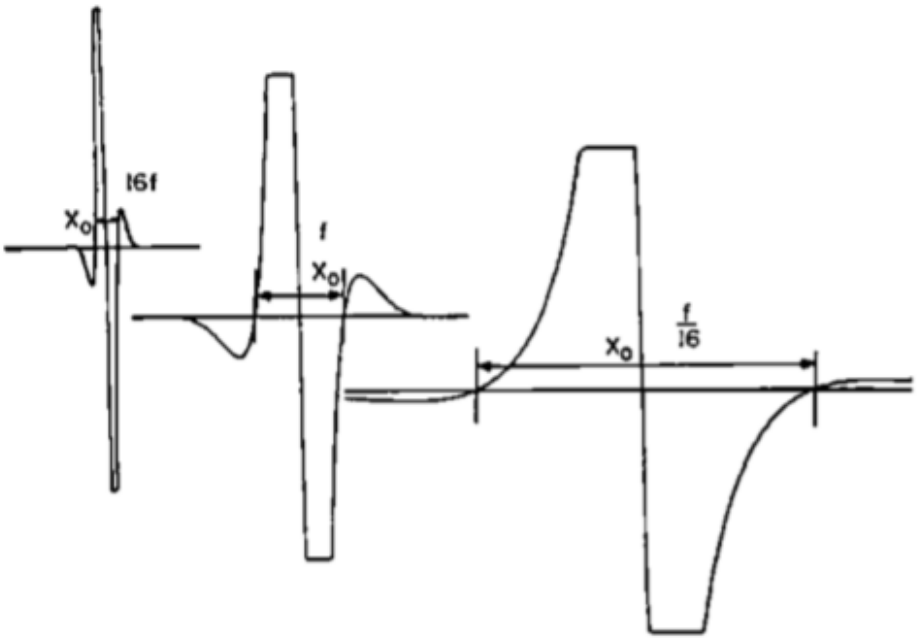

Figure 2.6: Plots of the real part of M_{tan} equation 2.26 as a function of the offset distance, x, between the probe and heating beam for three different frequencies [10, 15]

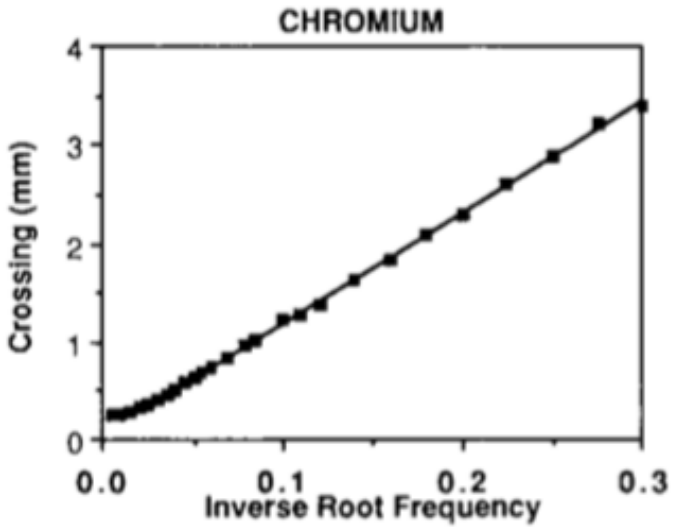

Figure 2.7: Experimental (squares) and theortical(line) plots of x_0 versus the reciprocal of the square root of the frequency for a pure single crystal of chromium [16]

making experimental measurements, that the low- frequency portion of this plot be used to calculate the slope. This is because we have assumed that the probe beam height, h, is small. "Small" in this case means compared to the thermal wavelength in air. The thermal wavelength increases with decreasing frequency, decreasing the effective height of the beam and making our assumption more valid. The high-frequency portions of both the theoretical and experimental curves show deviation from linearity associated with the finite beam height and the properties of the gas.

2.2.2 Layered Materials

The method used to measure the thermal diffusivity can also be applied to layered structures. This will be illustrated here by considering a material with a coating or an oxide on its surface. The theoretical description of the mirage effect for a coated material is very similar to the description of the uncoated material above. In the following, we extend the theoretical treatment to a more general case of situations. We will again let the subscript "g" indicate the gas above the surface, but will use the subscript "i" to indicate the layered material, rather than the bulk material under it. We can describe the layered material by simply adding more equations to equation (2.13).

$$\nabla.[\kappa_i \nabla \bar{T}_i(x,z)] + \kappa_i q_i^2 \bar{T}_i(x,z) = -\delta(x)\delta(z) \tag{2.29}$$

where we also use the Fourier transform as following

$$\bar{T}_i(x,z) = \int_{-\infty}^{\infty} dk e^{ikx} t_i(k,z) \tag{2.30}$$

which satisfies the differential equation

$$\frac{\partial}{\partial z}[\kappa_i \frac{\partial}{\partial z} t_i(k,z)] + \kappa_i k_i^2 t_i(k,z) = \frac{-1}{2\pi}\delta(z) \tag{2.31}$$

where

$$k_i = (q_i^2 - k^2)^{1/2} \tag{2.32}$$

With a corresponding addition to equations 2.13 and 2.16 the solution to 2.31 take the form

$$t_g(k,z) = C_g e^{-ik_g z}; z < 0(gas) \tag{2.33}$$

$$t_1(k,z) = C_1 sinh(O_1 + ik_1 z); 0 < z < a_1 \tag{2.34}$$

$$t_i(k,z) = C_i sinh(O_i + ik_i(z - a_{i-1})); a_{i-1} < z < a_i, i = 2,3,.... \tag{2.35}$$

The form of the equations (2.34) and (2.35) was chosen to include waves propagating in both positive and negative directions. This is because the wave propagating away from the source (at z=0) will now scatter at each of the boundaries between two adjacent layers at $z = a_i$. The constant C_g describes the amplitude and phase of the thermal waves propagating into the gas. This wave is the one that is responsible for the deflection of the probe beam that gives rise to the mirage signal. The complex constant O_1 describes the relative amplitude and phase between forward-going and backward-going waves in layer 1. With the only source at z=0, this quantity describes the collective response to a forward-going thermal wave of all layers in the half-space z>0. Indeed, when we apply the boundary conditions as before at z=0, we obtain

$$C_g = C_1 sinh(O_1) \tag{2.36}$$

and

$$i\kappa_g k_g C_g + i\kappa_1 k_1 C_1 cosh(O_1) = \frac{-1}{2\pi} \tag{2.37}$$

The value of the constant C_g is all that is necessary to describe the temperature distribution in the gas, and hence to calculate the probe-beam deflection. If we combine both equations (2.36) and (2.37) we get the following

$$C_g = \frac{i}{2\pi(\kappa_1 k_1 coth(O_1) + \kappa_g k_g)} \tag{2.38}$$

Now, we do the same procedure we did for the bulk to find the formula of transverse and normal deflection to get the following

$$M_{norm} = \frac{-1}{\pi}\frac{1}{n}\frac{dn}{dT} e^{-\frac{q_g^2 R_2^2}{4}} \int_0^{\infty} dk \frac{k_g cos(kx) e^{ik_g h} e^{-k^2 R_1^2/4}}{\kappa_1 k_1 coth(O_1) + \kappa_g k_g} \tag{2.39}$$

and

$$M_{tan} = \frac{-i}{\pi}\frac{1}{n}\frac{dn}{dT}e^{-\frac{q_g^2 R_2^2}{4}}\int_0^\infty dk \frac{ksin(kx)e^{ik_g h}e^{-k^2R_1^2/4}}{\kappa_1 k_1 coth(O_1) + \kappa_g k_g} \tag{2.40}$$

The value of O_1 can be determined if the value of O_2 is known, the value of O_2 can be determined if the value of O_3 is known, etc. This follow from the fact that the constant C_i can be eliminated from the boundary conditions at the interface between two successive layers [16].

$$tanh[O_i + ik_i(a_i - a_{i-1})] = \frac{\kappa_i k_i}{\kappa_{i+1}k_{i+1}} tanh(O_{i+1}) \tag{2.41}$$

In the following I will do the calculation only for thin films since my experimental measurements are based on thin films. Since the subscript "2" now refers to the substrate, which we shall consider to be thermally thick we set $tanh(O_2) = 1$. we get

$$O_1 = -ik_1 a_1 + tanh^{-1}(\frac{\kappa_1 k_1}{\kappa_b k_b}) \tag{2.42}$$

where the subscript "b" stands for the bulk substrate, and a_1 is the thickness of the thin film. With the resulting modified expression it is possible to extract information about the substrate as well as the thin film from experimental plots of M_{tan}. In this case, however, one needs more information than just the slope of x_0 versus $f^{-1/2}$. The full procedure is to make a multi-parameter fit of the real and imaginary part of M_{tan} formula with experimental results versus the offset distance, x. Depending on the magnitudes of the parameters involved, one can find any or all of the thin film thickness, thermal diffusivity, and thermal conductivity. These parameters can also similarly be found for the substrate. We can also find experimental parameters as probe beam height and radius of probe beam and heating beam. If some of the parameters are known from independent measurement the fitting process will be faster. Moreover, we should note that it's not necessary to use ultra-high frequencies to measure thin films. [10, 16].

Chapter 3

Description of The Experiment

The technique used in this experiment is to measure the transverse and normal deflection of the probe beam versus the distance x between the probe beam and the heating beam. In order to measure the following data we designed the experiment schematized in figure (3.1).

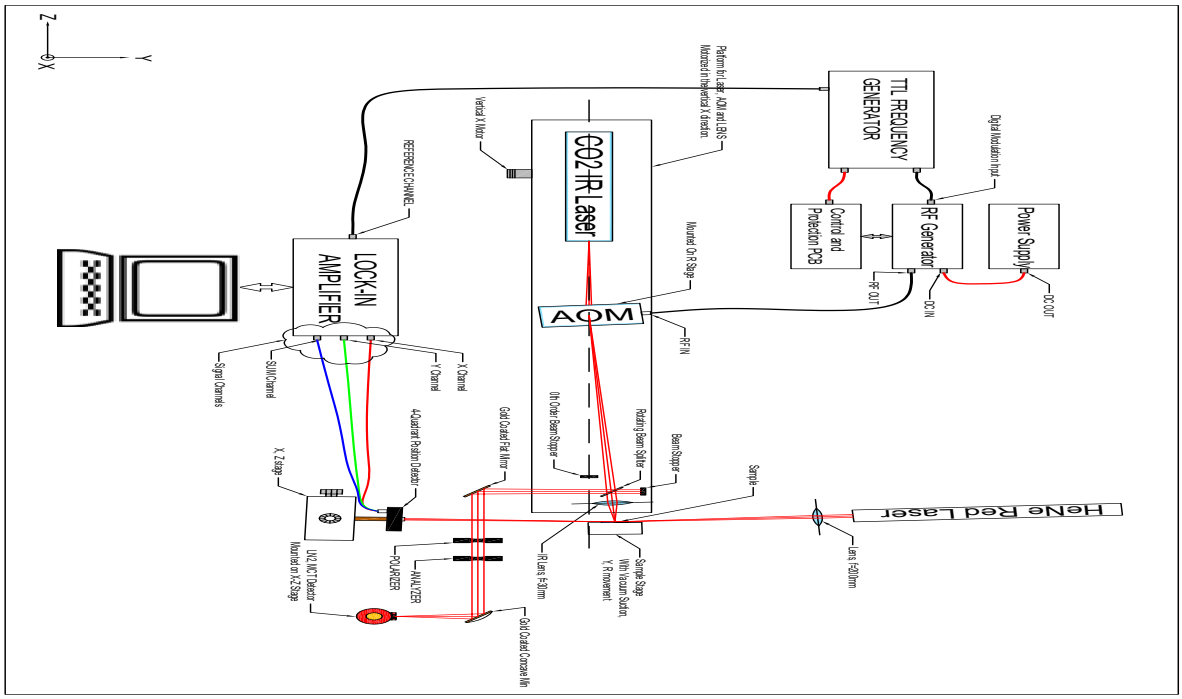

Figure 3.1: Schematic diagram of the experimental setup.

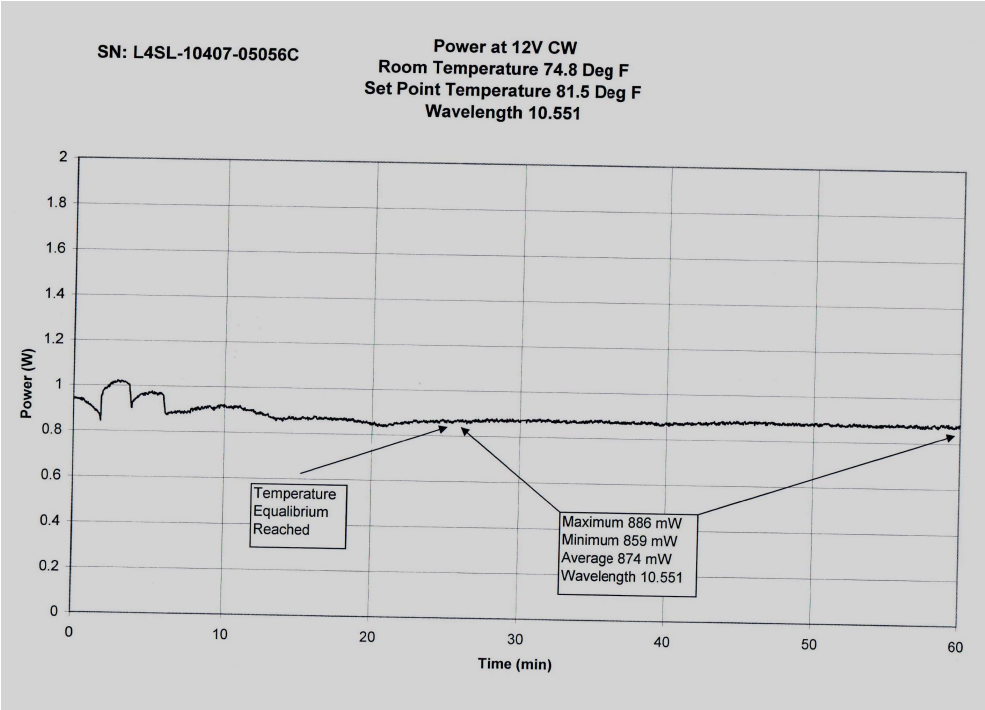

Figure 3.2: Power versus time of laser at $81.5°F$

3.1 Building the Experiment

In the following sections, we will describe in details the procedures of building the experiment.

3.1.1 Heating Beam

For the heating beam, we use a continuous CO_2 laser infrared laser, with an operating power of 1 watt. The wavelength is temperature dependent. It can be varied in the range $10.3-10.8$ μm. The beam waist diameter is 2.4 mm, the full divergence angle is 5.5 mrad, and it is horizontal linear polarized. In our experiment we set the laser temperature to 81.5 °F. This temperature produces a wavelength $10.551\mu m$. As shown in figure (3.2), the stabilization of the laser requires 25 minutes. The use of an infrared laser gives us the advantage that the measurment will not be affected by the surface roughness it doesn$'$t see the surface roughness. To make this laser stable, we should maintain the laser temperature at 81.5 °F. Therefore, the laser is connected to an air cooling system as shown in figure (3.3).

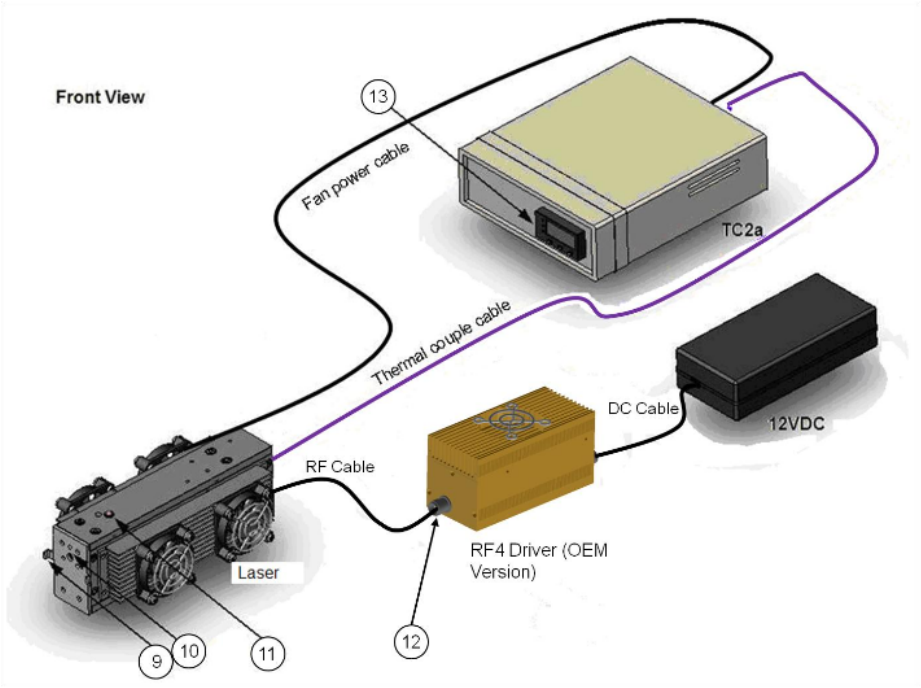

Figure 3.3: Laser system connection diagram

3.1.2 Modulation of the Heating Beam

The laser is in continuous wave mode. According to the theory of mirage effect, the heating beam should be modulated with a specific frequency. For this reason, the laser beam passes through an AOM (acousto-optic modulator). The AOM allows the intensity of light to be controlled and modulated at rates that far exceeding 70 KHz. The AOM is optimized for low scatter and high laser damage threshold. The rise time, modulation rate, beam diameter, and power handling needs of our application were studied carefully to identify the best AOM and RF(Radio Frequency) driver solution. An AOM uses sound waves within a crystal to create a diffraction grating. As the power of the applied RF signal is varied, the amount of diffracted light varies proportionally. Modulators can be used like a shutter (cycling light on and off at a set frequency), or as a variable attenuating value. (controlling the intensity of transmitted light dynamically). The most important factor in selecting a modulator is the required speed. This influences the choice of material, modulator design, and RF driver to be used. The speed of a modulator is described by the rise time, which determines how quickly the modulator can respond to the applied RF driver, and limits the modulation rate. The rise time is proportional to the time required for the acoustic wave to traverse the optical beam. Therefore, it is influenced by the beam diameter within the

modulator. The specifications of the used AOM is 10.6 µm wavelength, horizontal polarization, and numerical aperture up to 9.6 mm, which is adequete for the heating laser beam. Moreover, water is passing throught the AOM and its RF generator for cooling. Water is cooled by a chiller to keep the temperature fixed around 19°C. We have two diffracting beams from the AOM the zeroth and first order. The zeroth order beam is a beam modulated between 700 mW and 100 mW. The 100 mW would keep heating the surface of the sample which contradicts the theory of mirage-effect. Therefore, can′t be used in our measurement. The first order beam is modulated between 700 mW and 0 mW, which is convenient for our measurement.Hence we stop the zeroth order from hitting the sample, and we use only the first order beam. AOM is mounted on a stage for purpose alignment where we maximize the first order by measuring the intensity using an infrared power meter. The frequency is controlled by a square wave function generator.

3.1.3 Focusing the Heating Beam

The heating beam then passes through an infrared converging lens of 3 cm focal length that focuses the heating beam diameter to a 71 µm diameter. The sample surface is at exactly 3cm from the center of the lens. However, it is hard to put the sample exactly at 3 cm from the lens. This uncertainty affect the value of the heating beam diameter on the sample which is an important factor for the normal and transverse deflection. An accurate method to focus the heating beam was devised. We measure the reflectance of the infrared laser which gives an image of the spot temperature. The maximum reflectance means a maximum temperature and thus a minimum heating beam size spot. In order to measure the reflectance we emloyed a beam splitter as shown in figure (3.1). The reflected beam from the sample is reflected again by the beam splitter as shown in the figure (3.1). The reflected beam is measured by means of an infrared detector. A polarizer and an Analyzer are placed before the detector in order to control and keep it below 1 mW to avoid damaging the IR detector. The laser beam is focused by changing the position of the sample holder untill the maximum reflectance is reached. The signal of the detector is measured using a lock-in amplifier that measures only the modulated signal with frequency of the heating laser beam to avoid measuring errors of external infrared radiations.

3.1.4 Probe Beam

We use a He-Ne laser as a probe beam with 632.8nm wavelength, 5mW power, 0.81 mm beam diameter, and 1 mrad beam divergence . We focus the probe beam using a 20 cm focal length lens to achieve a 100 µm probe beam radius on the surface of the sample. The most challenging part in the experiment is the alignment of the probe beam with the heating beam because the heating beam

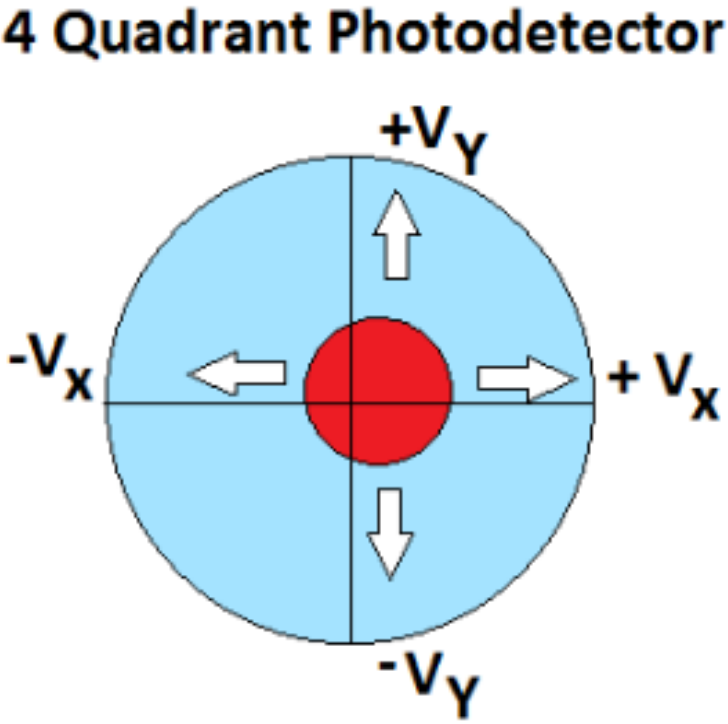

Figure 3.4: Position Sensing Quadrant Detector

is infrared. We found a convenient way that helps us in the alignment. We check whether the signal of the transverse deflection is antisymmetric or not.

3.1.5 Detection the Deflection of the Probe Beam

The reflected beam from the sample surface is directed to a Position Sensing Quadrant Detector that can be used to measure the deflection of the probe beam. The importance of this detector as shown in figure (3.4) is that it can measure normal and transverse deflections of the probe beam simultaneously. The detector operates in the wavelength range between 400 and 1100 nm, and for spot size diameter less than 3.9 mm. We mounted the detector on a stage for alignment at the minimum signal before heating as depicted. Figures (3.5) and (3.6) indicates that the probe beam is not at the center of the detector, which implies deflection by the heat waves.
The probe beam should be at the center of the detector before any measurement, the shutter of the heating laser is then opened and probe beam deflects. However, the signal of the detector passes through a lock-in amplifier that is referenced to the frequency of the modulated heating beam as shown in figure (3.5) and (3.6). Here we can see the importance of the lock-in amplifier in neglecting noise signals during measurement. Furthermore, the deflection is a horizontal straight

line which is an experimental verification that the deflection is not a function of the temperature. The heating beam is scanned along the sample surface in the vertical direction since we need the deflection versus, x, which is the distance between the heating beam and the probe beam. For that reason the laser, AOM and the lens system are mounted on very sensitive stages, with an error around 1 μm, to scan the sample in the vertical direction.

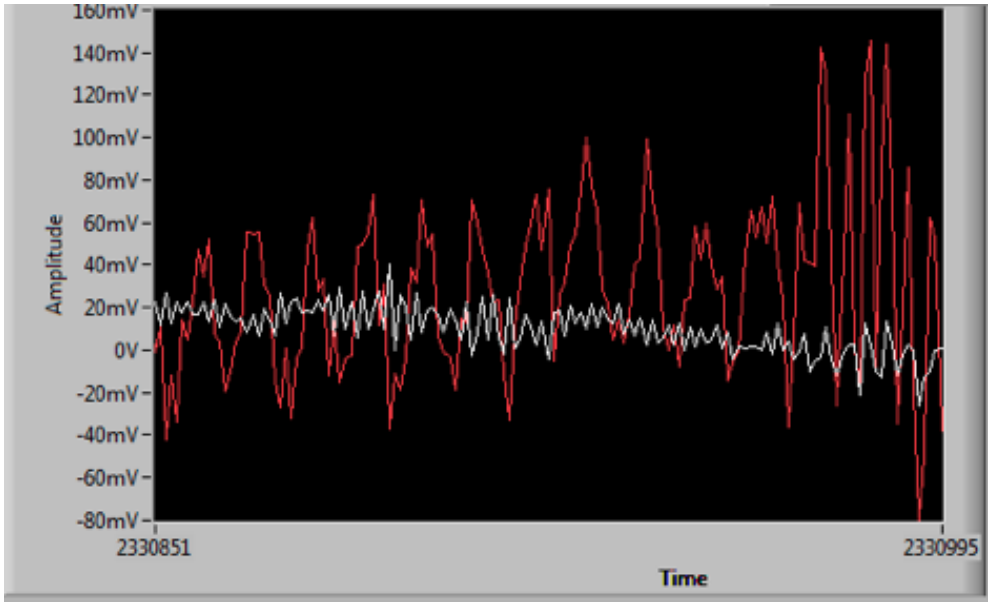

Figure 3.5: The graph shows the signal before passing to the lock-in amplifier

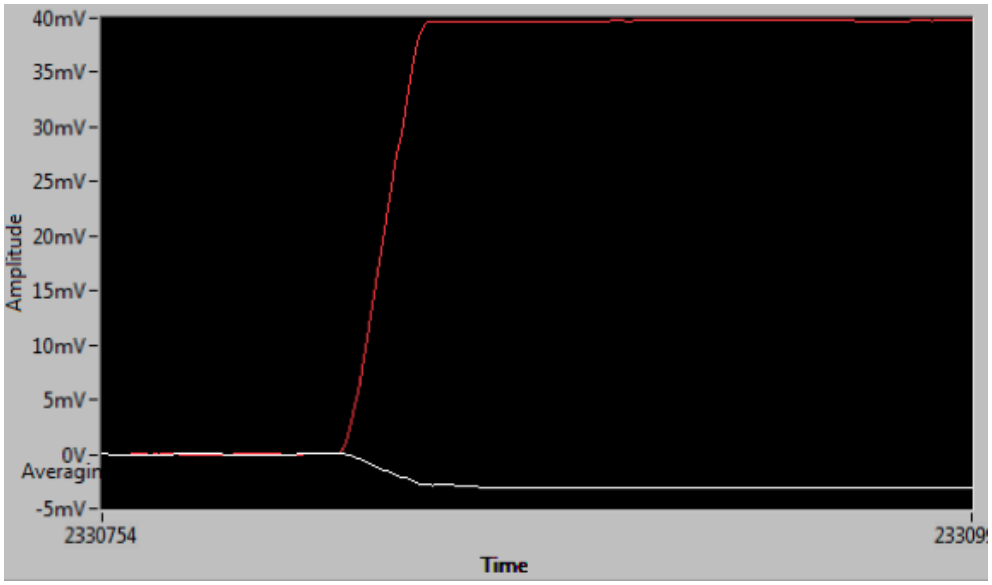

Figure 3.6: The graph shows the signal after passing to the lock-in amplifier

3.1.6 Verification of the Experiment

The last part of the experiment is to verify the results against theoretical graphs. The experiment is working properly and this shown in the measurement of the normal and transverse deflections of Silicon carbide sample with 4000 Hz modulation frequency where we see the shape of experimental results shown in figures (3.7) and (3.8) matches the theoretical results shown before in figures (2.4) and (2.5).

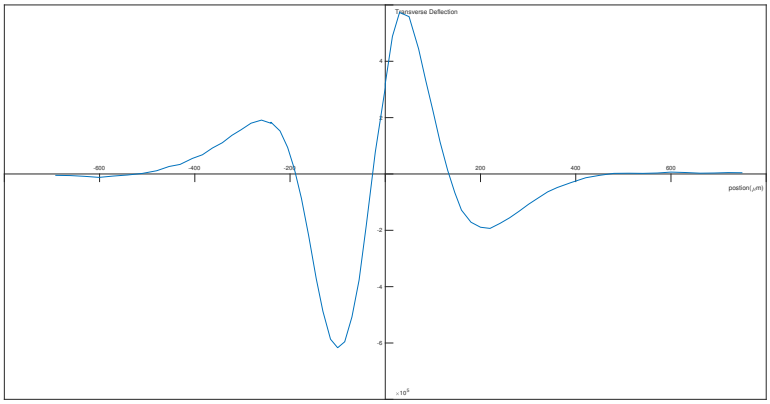

Figure 3.7: The experimental measurement of the real part of the transverse deflection versus the offset distance x

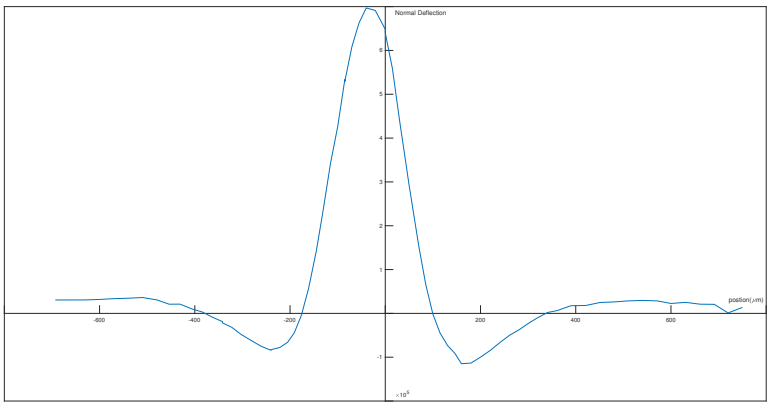

Figure 3.8: The experimental measurement of the real part of the normal deflection versus the offset distance x

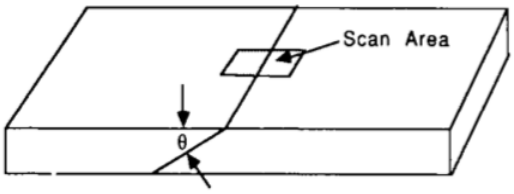

Figure 3.9: Geometry for a tightly closed, model slanted crack. The shaded region represents the area on the top surface, intersected by the crack, which is scanned by the heating beam in thermal wave imaging [16].

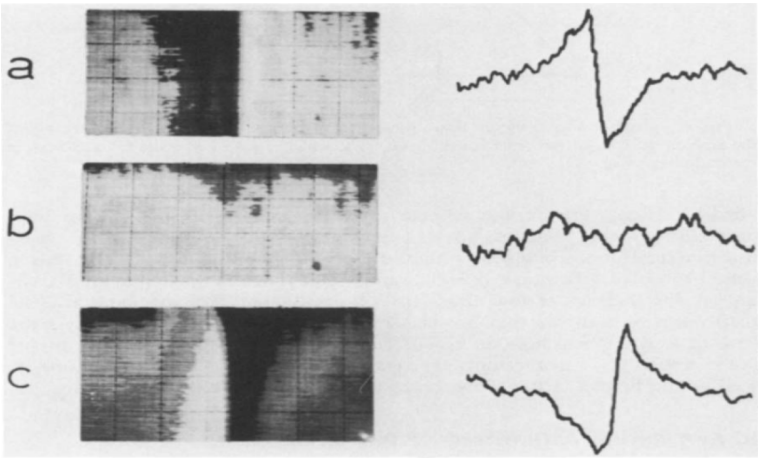

Figure 3.10: Mirage-effect thermal wave images and corresponding line scans for a fabricated vertical crack $\theta = 90$ in figure (3.9), using the variations in magnitude of normal deflection. (a) The heating beam is to the left of the probe beam; (b) the heating and probe beams intersect, and (c) the heating beam is to the right of the probe beam [16].

3.2 Image of Surface and Subsurface defects in Solid

Another important application of the Mirage-Effect experiment is the detection of cracks in materials. However, this application is limited to samples with flat surface. The procedure for the experiment is the same as before but we don't scan the heating beam with respect to the probe beam. The probe beam and the heating beam are kept aligned, and sample position is scanned with respect to the intersection of the heating and probe beams while storing the amplitude and the phase of both signals. Figures (3.9) and (3.10) shows some results of the detection of cracks using mirage-effect experiment.

Chapter 4

Dynamic Heat Management and Heat Flux Switching Through Stresses

In this chapter, we present the application of the developed optical setup to the measurement of the effect of external stress on the thermal conductivity of 4H-silicon carbide. We investigate the possibility of dynamic heat measurement in bulk materials and the development of bulk material based thermal switch through the application of external stresses.

4.1 Static and Transient Heat Transfer Management

The emergence of phononic in the last decades is the attempt to understand and control the thermal energy carried by phonons in a beneficial way. One can categorize two approaches to this task. The static and the dynamical approach. The static approach has demonstrated to be useful and efficient when it comes to problems related to thermoelectric, for instance. One strategy consists in introducing localized mass fluctuations through adding impurities or by alloying and nanostructuring [27]. The goal of introducing point defects or alloying is to increase the scattering of phonons. The phonon scattering rate will certainly depend on the energy of the phonon and the temperature of the sample. These static approaches are usually employed in thin films and bulk dielectric materials. Other static approaches of heat transfer control and management involve phonon confinement and localization, which are mechanisms that manifest themselves in nanostructures and superlattices. Surprising values of thermoelectric figure of merit have been achieved using these static approaches, and the topic remains an object of intensive research [28].

Although static tailoring of the phonon heat transfer is of utmost need and importance for many technological applications, dynamic management of heat transfer can open the door for interesting technologies. For instance, dynamic heat management can be well suited for system that are required to adapt to their surroundings. For example, recent research for developing phonon analogue to the electric diode, memory, transistor would allow for applications such as heat-based data storage or smart thermoelectric devices capable of adjusting their thermal properties to the temperature of the environment. Other examples involve devices and systems that can change their thermal properties when they are subject to different heat load. Component heating in electronic systems, ultimately, is dependent on the load of the task, and such heat loading is essentially of a transient character. Hence, transient thermal transfer management lends itself naturally in this case.

Some recent research works on thermal rectification approached the idea of transient heat management [29]. However, the observed thermal rectification coefficients were very small for potential integration in applications. Phase change materials have shown electrically controlled fast nanoscale heat flux modulation [30]. Significant contrast of heat flux has been observed due to the interplay between radiation heat transfer at the nanoscale and phase change materials. Furthermore, is was demonstrated that active and fully reversible control of thermal transport in a solid-state device can be achieved using ferroelectric thin films.

Strain has also been used to modify the thermal conductivity dynamically. Large reversible changes in thermal conductivity on the order of 70% could be achieved using only 2% mechanical strain due to the change in the density of twin-boundaries in thin films [31]. The increase in twin-boundary density has been shown to vary concurrently with the thermal conductivity. It was also shown that thermal conductivity could be modified in zinc oxide (ZnO) nanorods by the application of strain fields. Under high strain values (values exceeding the elastic limit), the phase change from wurtzite structure to another hexagonal structure induces a change in the thermal conductivity by a factor of almost two [32]. Such effects could be exploited in the development of non mechanical thermal modulators. Many studies have also shown that strain can be effective in changing the heat transfer in nanostructures and bulk crystals. Our objective for this thesis is to try and see whether it is possible to design a thermal switch. In other words, our objective is to try and see whether it is possible to control the thermal conductivity of a material using low values of stain, i.e., values that do not exceed the elastic limit. Hence, we are interested in systems whose thermal conductivity can be modified by external stresses, and recover their initial thermal conductivity value after removal of the external stresses.

4.2 Thermal Switch

A prototype model for mechanical thermal switch system was proposed in 2008. It is based on two contacts that can be brought together by mechanical actuation. The presence of a high-thermal conductivity material in between the substrates changes the thermal resistivity of the system when the two contacts touch. The design based on liquid metal droplets had shown superior "on/off" ratio than other designs. The "on/off" ratio of the liquid metal based switch was 1:100. The applicability of such a thermal switch into technological systems has not been considered. Although such systems have high efficiency when it comes to "on/off" ratio, they suffer from some size impracticalness and from operational degradation.

Other models for thermal switches come from recent investigations into the effect of strain on thermal conductivity. The reported results show that for low temperatures antimony doped germanium present a large increase in thermal conductivity when tensile strain is applied in some crystallographic directions. The theory of phonon scattering by donors predicted the magnitude and effect of applying strain which modified the electronic band structure of the antimony donors in the crystal. Amorphous silicon thermal conductivity also showed sensitivity to strain. By coupling an 50nm thick amorphous silicon film to a MEMS actuator, it was possible to apply large tensile strain to the film and demonstrate a decrease in thermal conductivity by a factor of 8. This fact was attributed to strong phonon localization in amorphous structures which is not present in crystalline silicon. This observation was not in line with experiments performed on thin films of silicon nitride that demonstrated that residual stress has no effect neither on the specific heat nor on thermal conductivity.

More recent studies showed that the thermal conductivity of 200nm amorphous silicon nitride can be increased upon mechanical loading up to 2.5% [33]. This contrasting result to the previous experiment was explained through possible changes in microstructure or carrier density.

Overall, it is clear that the topic of tailoring thermal conductivity using mechanical strains exhibits significant variability and promise. This opens up large possibilities for study and experimentation to build a thermal switch system.

As a theoretical ideal component, the thermal switch is a system that should have dynamic thermal conductivity. When the switch is in the on state, thermal energy flow is nominal, i.e., the component is a good conductor of heat. In the off state, the component acts as a thermal insulator. The switch can be triggered by applying strain to the material. This strain can be applied using an external electric field if the material is piezoelectric. It would also need to have response and high "on/off" ratio to be applicable with efficiency.

4.3 The effect of strain on thermal conductivity of dielectrics

One essential phonon scattering mechanism that we would like to discuss briefly before presenting our results is the phonon scattering by a strain field. The relaxation time associated with elastic strain field scattering of phonon modes has been first studied by Carruther in 1959 using second order perturbation theory [34]. He found that the effect of the Fourier component of the strain field is similar to that of the potential. This is somehow expected as phonons can be regarded as mechanical waves generated by lattice vibrations or localized strains. The application of the theory to edge dislocations at low temperature shows that the rate at which phonon scatter by strain is proportional to the density of dislocations and to the wave vector magnitude. The author also derived a Boltzmann like equation for the change in the phonon distribution due to the interaction of phonon with strain field.
In what follows, we study the effect of strain induced by proton bombardment on the thermal conductivity of silicon carbide. We use the infrared laser flash described previously to measure the thermal properties of the bombarded samples. Then, from the obtained results, we deduce the dependence of silicon carbide on strain in the limit of weak strain fields. Finally, we derive the dependence of silicon carbide thermal conductivity on external stress in the elasticity limit. We demonstrate that bulk silicon carbide can be used for thermal switch applications with "on/off" ratio of approximately 10%.

4.4 Results and Discussion

The thermal conductivity and thermal diffusivity of intact and bombarded 4H-silicon carbide substrates, as deduced from fitting the transverse deflection equation to the data obtained from the infrared laser flash experiment, are illustrated in figure(4.1). The fitting of the experimental data is presented in the Appendix. We note here that the measurements were carried out at eight laser modulation frequencies (3, 4, 4.5, 5, 6, 7, 9, and 12 kHz), however we show in each figure in the Appendix curves corresponding to three frequencies only for the sake of clarity.
The thermal conductivity and thermal diffusivity of the intact substrate are found to be 10.99 $W.K^{-1}.cm^{-1}$ and 4.6 $cm^2.s^{-1}$, respectively, which are in perfect agreement with the reported thermal properties of 4H-silicon carbide. The energy of the accelerated protons was 3meV. For that energy, the damage is expected to be concentrated at a depth of $60 \pm 5 \mu m$. The only variable was the dose of the irradiation. We have gradually varied the irradiation dose until we obtained observable effect on the thermal properties of the bombarded substrate. The threshold dose at which we observed effect on the thermal properties of the bombarded sub-

strate was approximately 10^{13}proton/cm^2. As can be noticed from figure(4.1), for a dose of approximately 10^{13}proton/cm^2, both the thermal conductivity and thermal diffusivity reduce by approximately 10%. However, when the irradiation dose doubles, the thermal conductivity drops rapidly while the thermal diffusivity drops with a smaller rate.
By definition, the thermal conductivity κ is given by

$$\kappa = \rho c_p \alpha \tag{4.1}$$

where ρ is the material mass density, c_p is the material specific heat at constant pressure, and α is the thermal diffusivity. Given that all the silicon carbide polytypes, which correspond to different silicon and carbon ions configurations with comparable energies within a unit cell, have the same specific heat, we can reasonably consider that irradiations with low doses induce weak variation in the ions configuration and crystal energy and do not affect the material specific heat. Hence, it will be possible to deduce the variation in the thermal conductivity versus the relative variation in the volume per atom, i.e., the variation in the thermal conductivity versus the strain.
Assuming unaffected specific heat by irradiations of low doses, equation(4.1) can be used to derive the following expression for strain field induced by irradiations of small doses,

$$\frac{\Delta V}{V_0} = strain = \frac{\Delta \alpha}{\alpha_0} - \frac{\Delta \kappa}{\kappa_0} \tag{4.2}$$

where$V_0, \alpha_0, and \kappa_0$ are the volume per atom, heat diffusivity, and thermal conductivity of the intact substrate. At this point, it is possible to plot the thermal conductivity versus strain up to a strain of 3% that correspond to the threshold irradiation dose. This threshold strain is the point between the elastic and plastic regimes. The linear relations between the physical quantities in the elastic regime allow us to assume that in the elastic regime, the thermal conductivity is linearly proportional to strain. The figure inset figure(4.1) presents the thermal conductivity versus strain within the elastic limit as calculated under the assumptions presented above. The positive values of imply that the strain induced by irradiations of ΔV low doses is a tensile strain.
On the other hand, for small deformation, we can express the strain as a function of external stress

$$K = \frac{stress}{strain} \tag{4.3}$$

where K is the silicon carbide bulk modulus, which is 250 GPa. Upon using equation(4.3), we can plot the thermal conductivity of 4H-silicon carbide versus external stress.
The thermal conductivity of 4H-silicon carbide versus external stress within the elasticity limit is presented in figure(4.2), which shows that it is possible to reduce the thermal conductivity of 4H-silicon carbide by approximately 10% by exerting

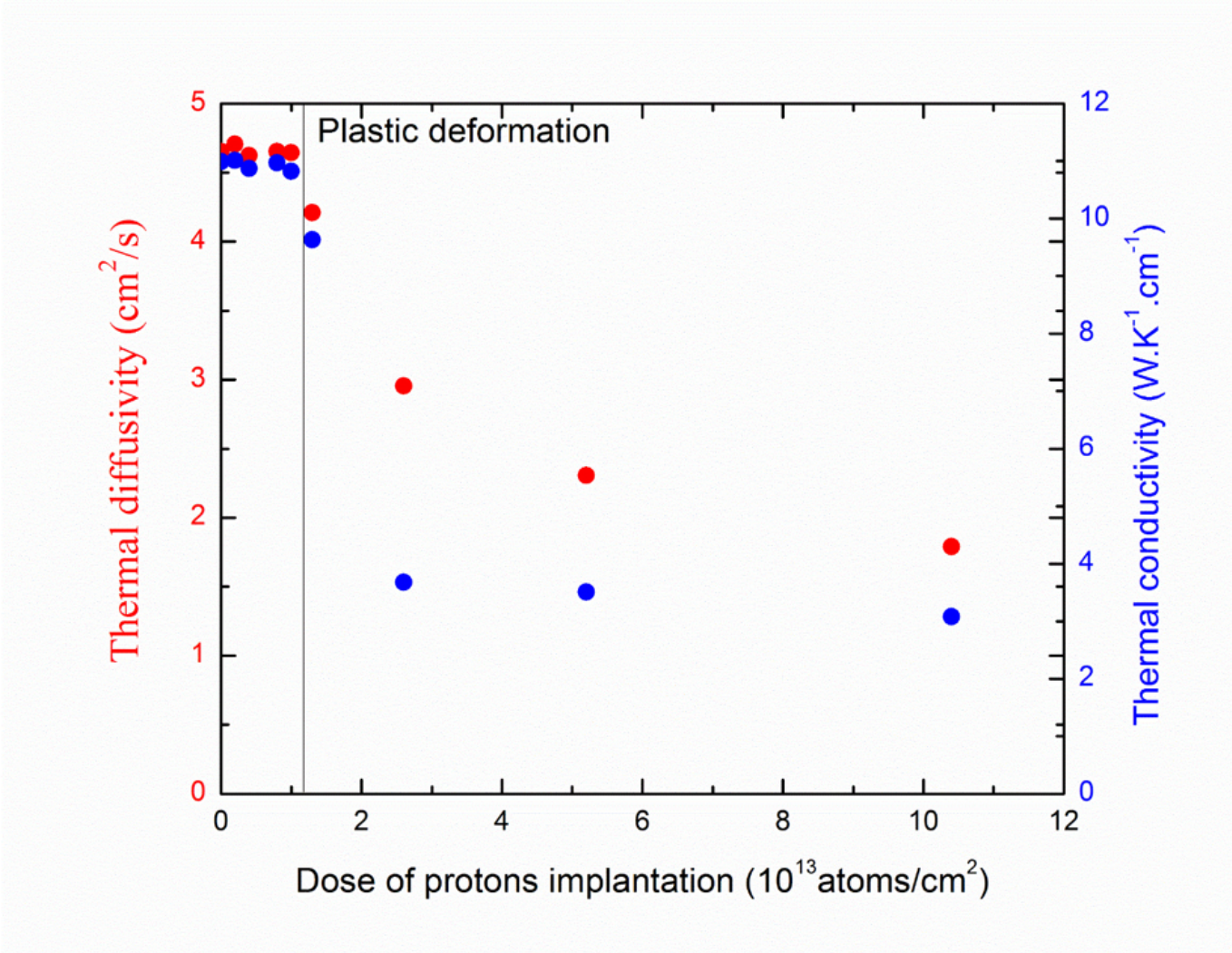

Figure 4.1: Thermal conductivity of 4H-silicon carbide versus protons implantation dose. Inset: Thermal conductivity of 4H-silicon carbide versus strain.

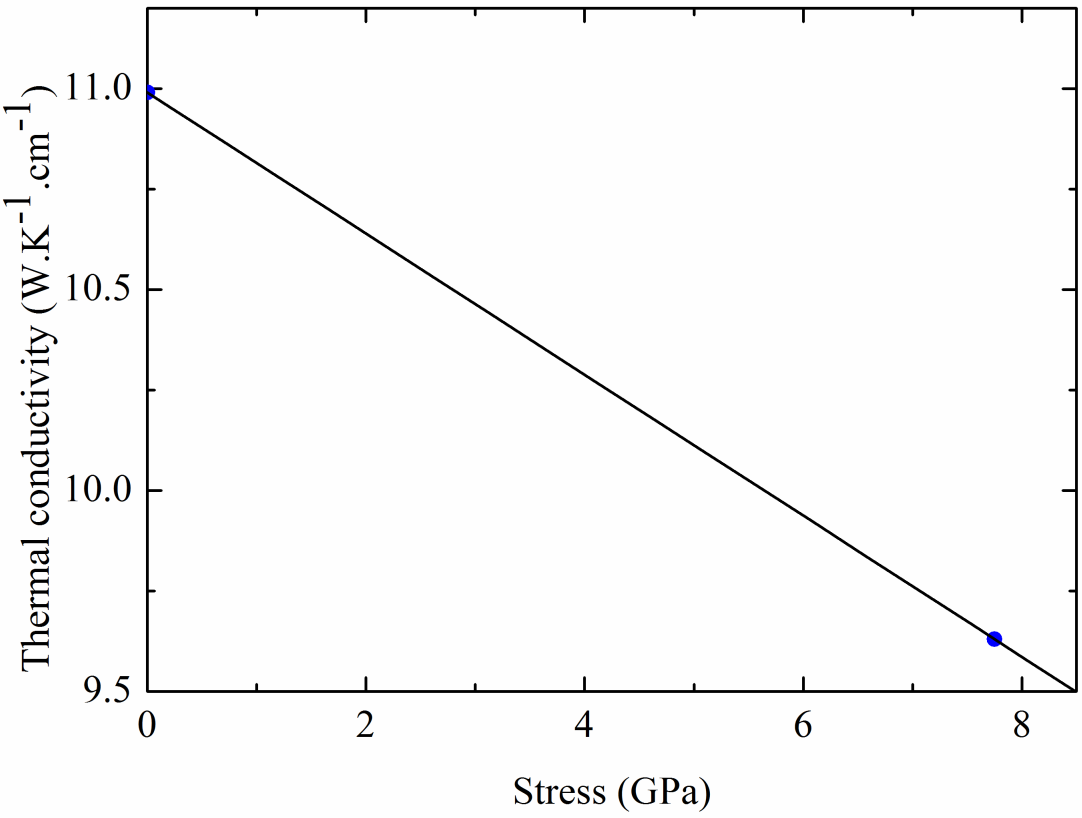

Figure 4.2: Thermal conductivity of 4H-silicon carbide versus stress within the elasticity limit.

weak stresses. In other words, the results presented in figure(4.2) demonstrate that dynamic tailoring of thermal conductivity in bulk 4H-silicon carbide through the application of weak stresses is possible. Nevertheless, the application of these findings to thermal switch would result in "on/off" ratio of only 1.15.

Chapter 5

Future Work

In our thesis, we measure the thermal conductivity and thermal diffusivity for substrate materials using mirage-effect. We are working to expand the experiment to measure also the heat capacity. Moreover, this experiment can also be applied to layered materials to measure thermal properties of thin films as shown in section (2.2.2). We can do multiparameter fit for the experimental data with the theoretical expression of equations (2.39) and (2.40).

5.1 Measuring Heat Capacity Using Mirage-Effect Experiment

One of the important ideas that came to our mind when we were focusing the heating beam as shown in section (3.1.3) is that the reflectance from the sample can be used as thermometer for the temperature of the sample, and the reflected beam from the beam splitter gives information about the transmitted power to the sample, so for each power we can find the temperature. From this information we can deduce the heat capacity of the material by making an extension to the experiment as shown in figure(5.1). Moreover, the AOM (acousto-optic modulator) has an option in monitoring the power of the heating beam. The main idea is to vary the power and measure the temperature at each instant by heating the sample then cooling it by increase the power of the heating beam then decreasing it to the minimum. Then, we do a fit for the power versus temperature with the expression that contains heat capacity to find it.

One of the important applications for this experiment is measuring all the thermal properties of the materials which are thermal conductivity, thermal diffusivity, and heat capacity at room temperature.

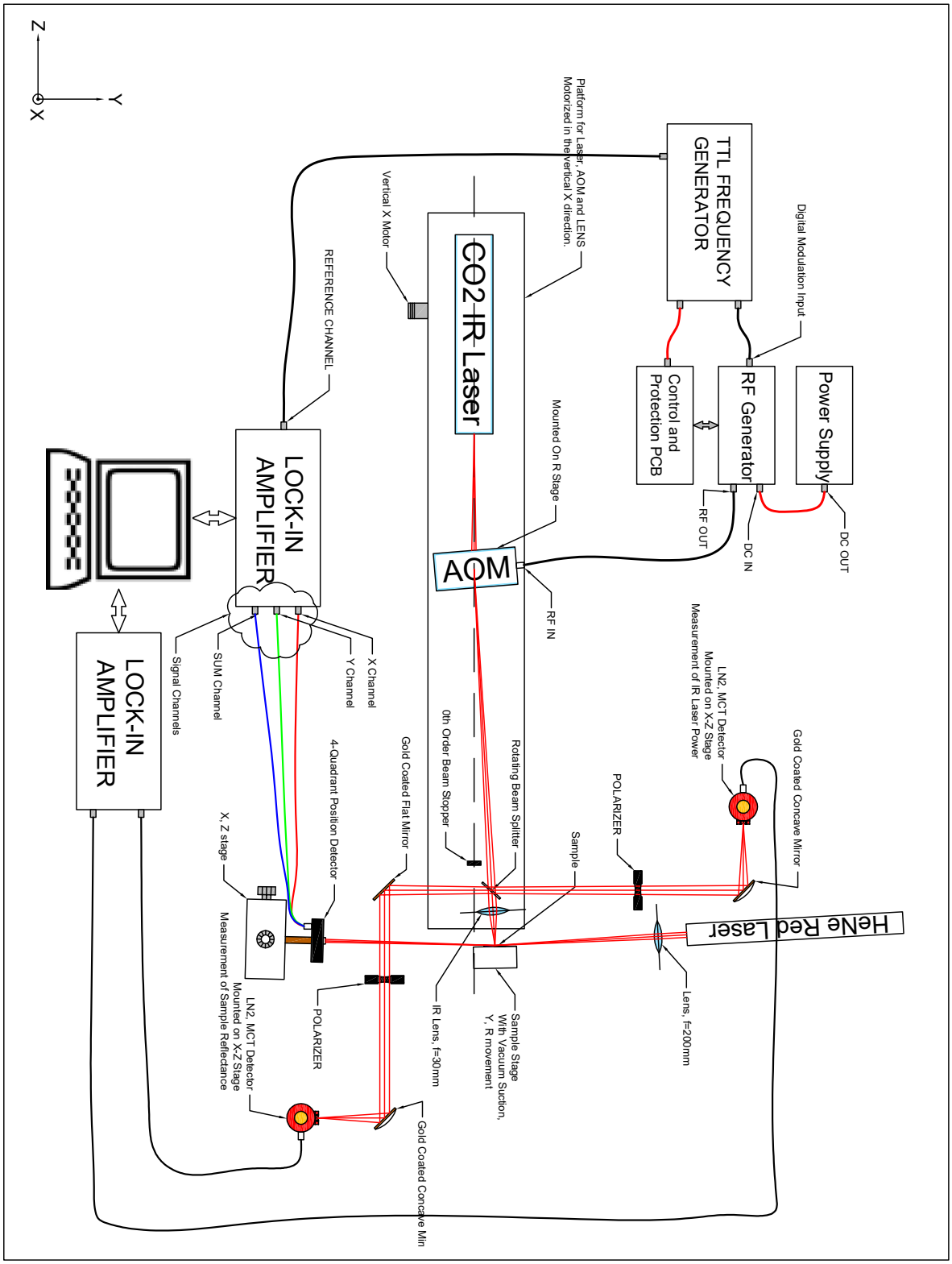

Figure 5.1: Schematic diagram of the expected experimental setup.

5.2 Conclusion

In the thesis discussed above we present measurements of thermal properties of materials using mirage-effect experiment where chapter one talks about thermal transport in general, chapter two describes the theory of mirage-effect experiment, chapter three describes building the mirage effect experiment, chapter four tackles the problem of heat flux in silicon carbide with external stress, and this chapter shows the future work that we want to do in the experiment.

Appendix A

Graphs

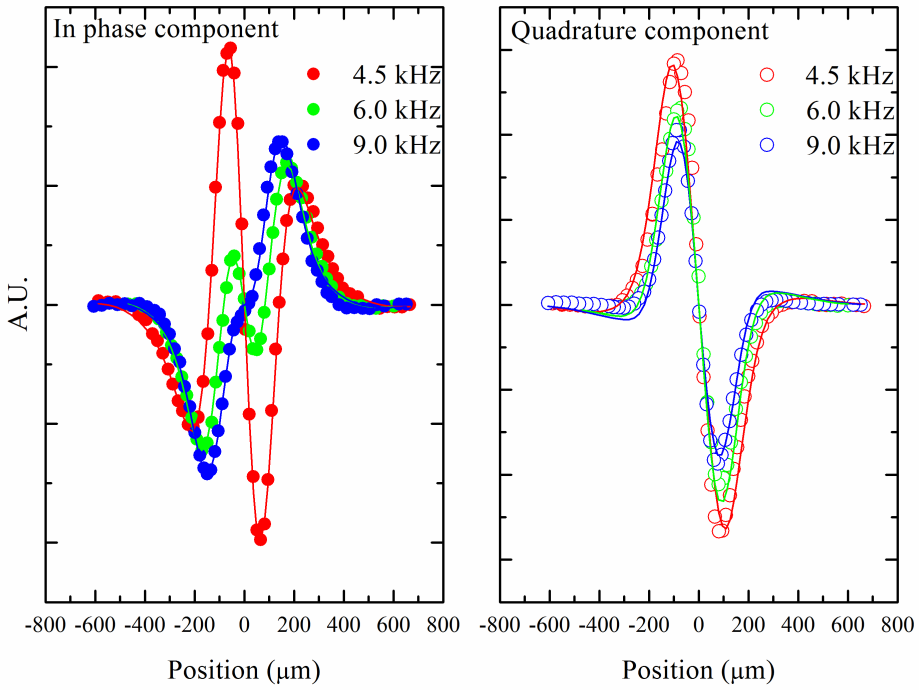

Figure A.1: Measurement and data fitting corresponding to the intact substrate. Symbols: measurements. Solid lines: data fitting. Measurements were carried out for eight different frequencies of heat beam modulation. However, curves corresponding to only three modulation frequencies are shown for the sake of clarity.

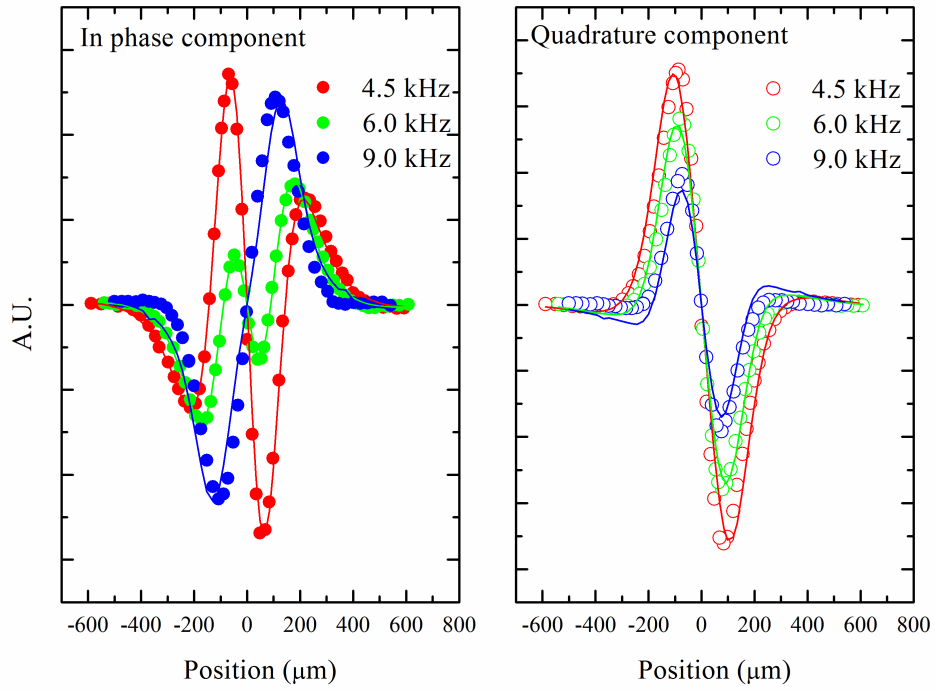

Figure A.2: Measurement and data fitting corresponding to the substrate irradiated with the threshold dose. Symbols: measurements. Solid lines: data fitting. Measurements were carried out for eight different frequencies of heat beam modulation. However, curves corresponding to only three modulation frequencies are shown for the sake of clarity.

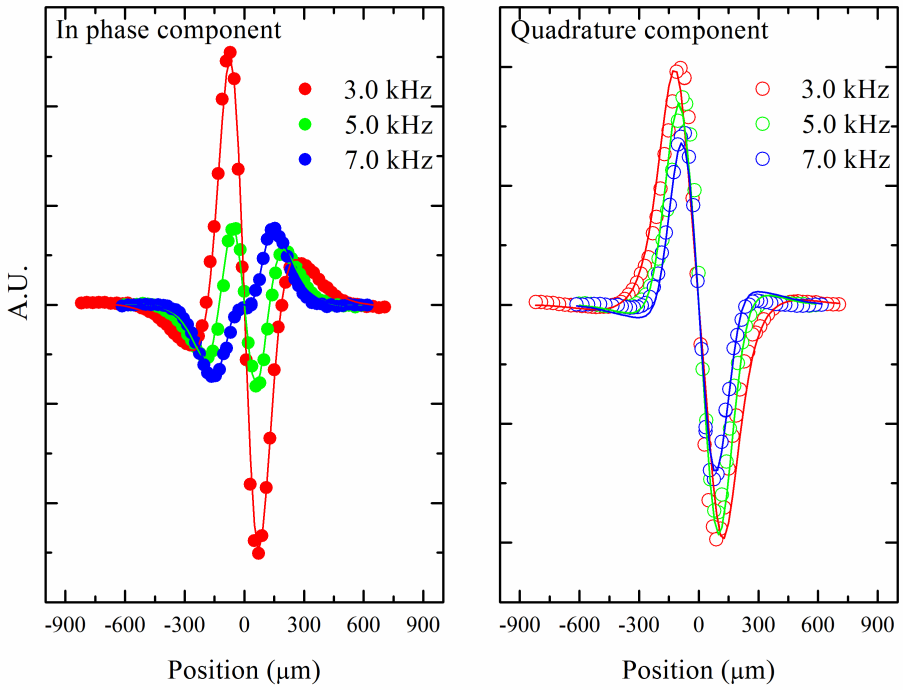

Figure A.3: Measurement and data fitting corresponding to the substrate irradiated with twice the threshold dose. Symbols: measurements. Solid lines: data fitting. Measurements were carried out for eight different frequencies of heat beam modulation. However, curves corresponding to only three modulation frequencies are shown for the sake of clarity.

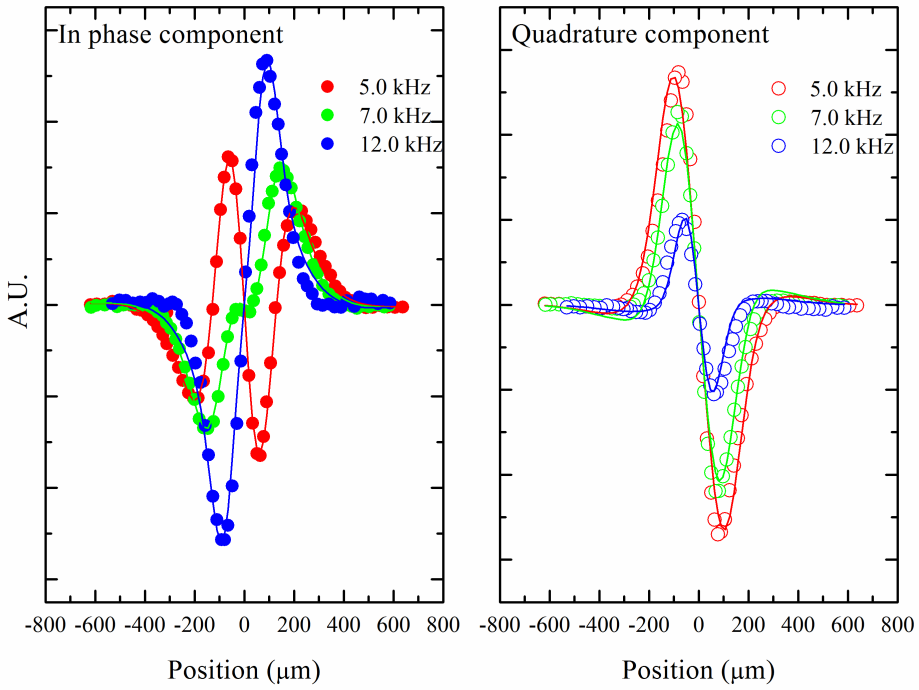

Figure A.4: Measurement and data fitting corresponding to the substrate irradiated with four times the threshold dose. Symbols: measurements. Solid lines: data fitting. Measurements were carried out for eight different frequencies of heat beam modulation. However, curves corresponding to only three modulation frequencies are shown for the sake of clarity.

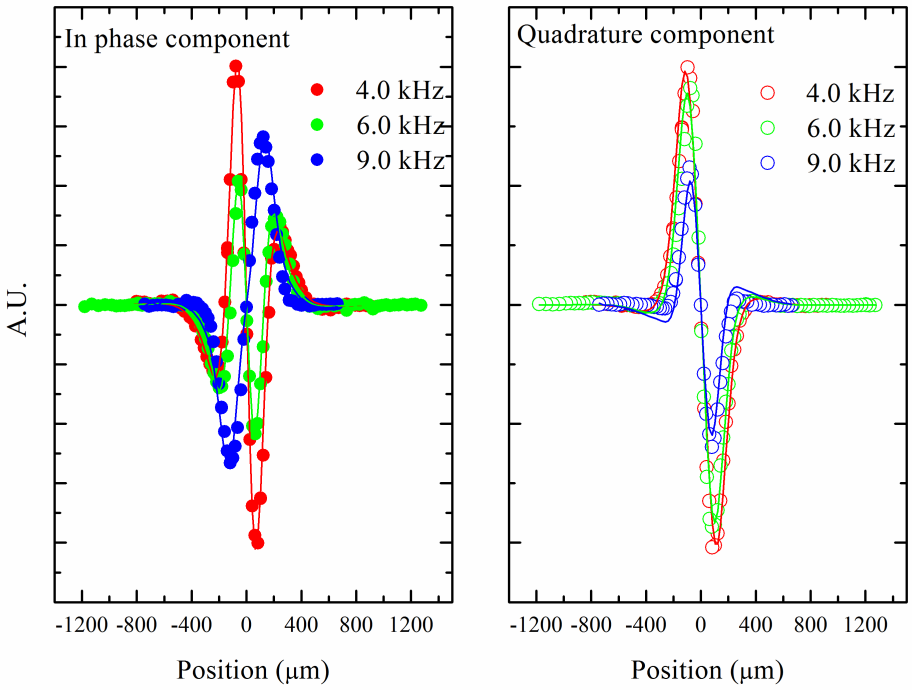

Figure A.5: Measurement and data fitting corresponding to the substrate irradiated with eight times the threshold dose. Symbols: measurements. Solid lines: data fitting. Measurements were carried out for eight different frequencies of heat beam modulation. However, curves corresponding to only three modulation frequencies are shown for the sake of clarity.

Bibliography

[1] G. Chen, *Nanoscale energy transport and conversion: a parallel treatment of electrons, molecules, phonons, and photons*. Oxford University Press, 2005.

[2] G. Pells, "Ceramic materials for fusion reactor applications," *Journal of Nuclear Materials*, vol. 123, no. 1-3, pp. 1338–1351, 1984.

[3] R. Thorne and V. Howard, "Radiation-induced changes in porous cubic silicon carbide.," tech. rep., United Kingdom Atomic Energy Authority, Culcheth, Eng., 1967.

[4] R. Price, "Effects of fast-neutron irradiation on pyrolytic silicon carbide," *Journal of Nuclear Materials*, vol. 33, no. 1, pp. 17–22, 1969.

[5] K. Minato, K. Fukuda, A. Ishikawa, and N. Mita, "Advanced coatings for htgr fuel particles against corrosion of sic layer," *Journal of nuclear materials*, vol. 246, no. 2-3, pp. 215–222, 1997.

[6] S. Sharafat, R. Jones, A. Kohyama, and P. Fenici, "Status and prospects for sic sic composite materials development for fusion applications," *Fusion engineering and design*, vol. 29, pp. 411–420, 1995.

[7] D. A. Bloore, *Reactor physics assessment of thick silicon carbide clad PWR fuels*. PhD thesis, Massachusetts Institute of Technology, 2013.

[8] H. Carslaw and J. Jaeger, "Conduction of heat in solids,(1959), 282."

[9] C. B. Reyes, "Thermal wave measurement of thermal diffusivities of solids.," 1988.

[10] A. Mandelis, "Photoacoustic and thermal wave phenomena in semiconductors," 1987.

[11] A. Boccara, D. Fournier, and J. Badoz, "Thermo-optical spectroscopy: Detection by themirage effect," *Applied Physics Letters*, vol. 36, no. 2, pp. 130–132, 1980.

[12] W. B. Jackson, N. M. Amer, A. Boccara, and D. Fournier, "Photothermal deflection spectroscopy and detection," *Applied optics*, vol. 20, no. 8, pp. 1333–1344, 1981.

[13] L. Aamodt and J. Murphy, "Thermal effects in photothermal spectroscopy and photothermal imaging," *Journal of applied physics*, vol. 54, no. 2, pp. 581–591, 1983.

[14] P. Kuo, M.-J. Lin, C. Reyes, L. Favro, R. Thomas, D. Kim, S.-y. Zhang, L. Inglehart, D. Fournier, A. Boccara, *et al.*, "Mirage-effect measurement of thermal diffusivity. part i: experiment," *Canadian journal of physics*, vol. 64, no. 9, pp. 1165–1167, 1986.

[15] P. Kuo, E. Sendler, L. Favro, and R. Thomas, "Mirage-effect measurement of thermal diffusivity. part ii: Theory," *Canadian Journal of Physics*, vol. 64, no. 9, pp. 1168–1171, 1986.

[16] P. Kuo, L. Favro, and R. Thomas, "Mirage detection of thermal waves," *Photothermal Investigations of Solids and Fluids*, pp. 191–212, 1988.

[17] J. Pezoldt, C. Zgheib, P. Masri, M. Averous, F. Morales, R. Kosiba, G. Ecke, P. Weih, and O. Ambacher, "Sims investigation of the influence of ge predeposition on the interface quality between sic and si," *Surf. Interface Anal*, vol. 36, pp. 969–972, 2004.

[18] M. Foygel, R. Morris, D. Anez, S. French, and V. Sobolev, "Theoretical and computational studies of carbon nanotube composites and suspensions: Electrical and thermal conductivity," *Physical Review B*, vol. 71, no. 10, p. 104201, 2005.

[19] B. Latour, *Contribution à l'étude du transport d'énergie dans la matière condensée: phonons, électrons et photons.* PhD thesis, Paris Saclay, 2015.

[20] S. Wei and M. Y. Chou, "Phonon dispersions of silicon and germanium from first-principles calculations," *Phys. Rev. B*, vol. 50, pp. 2221–2226, Jul 1994.

[21] M. Carvalho, A. Karydas, C. Casaca, C. Zarkadas, T. Paradellis, M. Kokkoris, B. Nsouli, and A. Cunha, "Fluorine determination in human healthy and carious teeth using the pige technique," *Nuclear Instruments and Methods in Physics Research Section B: Beam Interactions with Materials and Atoms*, vol. 179, no. 4, pp. 561–567, 2001.

[22] L. R. Doolittle, "Algorithms for the rapid simulation of rutherford backscattering spectra," *Nuclear Instruments and Methods in Physics Research Section B: Beam Interactions with Materials and Atoms*, vol. 9, no. 3, pp. 344–351, 1985.

[23] J. Callaway, "Model for lattice thermal conductivity at low temperatures," *Physical Review*, vol. 113, no. 4, p. 1046, 1959.

[24] M. Kazan and S. Volz, "Calculation of the lattice thermal conductivity in granular crystals," *Journal of Applied Physics*, vol. 115, no. 7, p. 073509, 2014.

[25] M. Kazan, E. Moussaed, R. Nader, and P. Masri, "Elastic constants of aluminum nitride," *physica status solidi (c)*, vol. 4, no. 1, pp. 204–207, 2007.

[26] S. H. Simon, *The Oxford solid state basics*. OUP Oxford, 2013.

[27] A. Iskandar, A. Abou-Khalil, M. Kazan, W. Kassem, and S. Volz, "On the interplay between phonon-boundary scattering and phonon-point-defect scattering in sige thin films," *Journal of Applied Physics*, vol. 117, no. 12, p. 125102, 2015.

[28] F. Suriano, M. Ferri, F. Moscatelli, F. Mancarella, L. Belsito, S. Solmi, A. Roncaglia, S. Frabboni, G. Gazzadi, and D. Narducci, "Influence of grain size on the thermoelectric properties of polycrystalline silicon nanowires," *Journal of Electronic Materials*, vol. 44, no. 1, pp. 371–376, 2015.

[29] C. Chang, D. Okawa, A. Majumdar, and A. Zettl, "Solid-state thermal rectifier," *Science*, vol. 314, no. 5802, pp. 1121–1124, 2006.

[30] P. Van Zwol, K. Joulain, P. B. Abdallah, J.-J. Greffet, and J. Chevrier, "Fast nanoscale heat-flux modulation with phase-change materials," *Physical Review B*, vol. 83, no. 20, p. 201404, 2011.

[31] K. D. Parrish, A. Jain, J. M. Larkin, W. A. Saidi, and A. J. McGaughey, "Origins of thermal conductivity changes in strained crystals," *Physical Review B*, vol. 90, no. 23, p. 235201, 2014.

[32] J. Cho, C. Richards, D. Bahr, J. Jiao, and R. Richards, "Evaluation of contacts for a mems thermal switch," *Journal of Micromechanics and Microengineering*, vol. 18, no. 10, p. 105012, 2008.

[33] M. Alam, R. Pulavarthy, C. Muratore, and M. A. Haque, "Mechanical strain dependence of thermal transport in amorphous silicon thin films," *Nanoscale and Microscale Thermophysical Engineering*, vol. 19, no. 1, pp. 1–16, 2015.

[34] P. Carruthers, "Scattering of phonons by elastic strain fields and the thermal resistance of dislocations," *Physical Review*, vol. 114, no. 4, p. 995, 1959.